1   **Impacts of aerosol-radiation interaction on meteorological forecast**

2   **over northern China by offline coupling the WRF-Chem simulated**

3   **AOD into WRF: a case study during a heavy pollution event**

5   Yang Yang[1], Min Chen[1], Xiujuan Zhao[1*], Dan Chen[1*], Shuiyong Fan[1],

6   and Shaukat Ali[2]

7   *1 Institute of Urban Meteorology, China Meteorological Administration, Beijing*

8   *100089, China*

9   *2 Global Change Impact Studies Centre, Ministry of Climate Change, Islamabad*

10   *44000, Pakistan*

Abstract

To facilitate the future inclusion of aerosol-radiation interactions in the regional operational Numerical Weather Prediction (NWP) system – RMAPS-ST (adapted from Weather Research and Forecasting, WRF) at the Institute of Urban Meteorology (IUM), China Meteorological Administration (CMA), the impacts of aerosol-radiation interactions on the forecast of surface radiation and meteorological parameters during a heavy pollution event (December 6th -10th, 2015) over northern China were investigated. The aerosol information was simulated by RMAPS-Chem (adapted from WRF model coupled with Chemistry, WRF-Chem) and then offline-coupled into Rapid Radiative Transfer Model for General Circulation Models (RRTMG) radiation scheme of WRF to enable the aerosol-radiation feedback in the forecast. To ensure the accuracy of high-frequency (hourly) updated aerosol optical depth (AOD) field, the temporal and spatial variations of simulated AOD and aerosol extinction coefficient at 550nm were evaluated against in-situ and satellite observations. Comparisons with in-situ and Moderate Resolution Imaging Spectroradiometer (MODIS), AErosol Robotic NETwork (AERONET), and Cloud-Aerosol Lidar and Infrared Pathfinder Satellite Observation (CALIPSO) satellite observations showed that the model could reproduce and spatial and vertical distribution as well as the temporal variation the of polluted episode. Further comparison of $PM_{2.5}$ with in-situ observation showed WRF-Chem reasonably captured the $PM_{2.5}$ field in terms of spatial distribution and magnitude, with the

32   correlation coefficients of 0.85, 0.89, 0.76, 0.92 and 0.77 at Beijing, Shijiazhuang,

33   Tianjin, Hebei and Henan, respectively. Forecasts with/without the aerosol

34   information were conducted further, and the differences of surface radiation, energy

35   budget, and meteorological parameters were evaluated against surface and sounding

36   observations. The offline-coupling simulation (with aerosol-radiation interaction

37   active) showed a remarkable decrease of downward shortwave (SW) radiation

38   reaching surface, thus helping to reduce the overestimated SW radiation during

39   daytime. The simulated surface radiation budget was also improved, with the biases

40   of net surface radiation decreased by 85.3%, 50.0%, 35.4%, and 44.1% during

41   daytime at Beijing, Tianjin, Taiyuan and Jinan respectively, accompanied by the

42   reduction of sensible (16.1 W m^{-2}, 18.5%) and latent (6.8 W m^{-2}, 13.4%) heat fluxes

43   emitted by the surface at noon-time. In addition, the cooling of 2-m temperature

44   (~0.40 °C) and the decrease of horizontal wind speed near surface (~0.08 m s^{-1})

45   caused by the aerosol-radiation interaction over northern China helped to reduce the

46   bias by ~73.9% and ~7.8% respectively, particularly during daytime. Further

47   comparisons indicated that the simulation implemented AOD could better capture

48   the vertical structure of atmospheric wind. Accompanied with the lower planetary

49   boundary layer and the increased atmospheric stability, both U and V wind at

50   850hPa showed the convergence which were unfavorable for pollutants dispersion.

51   Since RMPAS-ST provides meteorological initial condition for RMAPS-Chem, the

52   changes of meteorology introduced by aerosol-radiation interaction would routinely

53   impact the simulations of pollutants. To verify the statistically significance of the

54   results, we further conducted the 24-hour forecasts for a longer period lasting 27

55   days (Jan. 13th – Feb. 8th, 2017), with no AOD field (NoAero) and WRF-Chem

56   simulated hourly AOD fields (Aero) included, as well as constant AOD value of

57   0.12 (ClimAero), respectively. The one-month results were statistically significant

58   and indicated that the mean RMSE of 2-m temperature (wind speed at 10m) in Aero

59   and ClimAero relative to NoAero was reduced by 3.95% (1.86%) and 1.23%

60   (1.63%). More detailed evaluations and analysis will be addressed in a future article.

61   These results demonstrated the profound influence of aerosol-radiation interactions

62   on the improvement of predictive accuracy and the potential prospects to offline

63   couple near-real-time aerosol information in regional RMAPS-ST NWP in northern

64   China.

65   **Key words:** Aerosol-radiation interactions, offline-coupling, WRF, northern China,

66   pollution

1. Introduction

Aerosol-radiation interactions modify the radiative energy budget of the earth-atmosphere system through the interaction between aerosols and solar radiation by scattering and absorbing mechanism as well as the absorption and emitting of thermal radiation (Ramanathan et al., 2001; Yu et al., 2006). The aerosol-radiation interaction may cool or heat the earth-atmosphere system, alter surface and atmospheric radiation and temperature structure on regional and global climate, which have been widely reported and studied (Hansen et al., 1997; Ramanathan et al., 2001; Kaufman et al., 2002; Liao et al., 2006; Zhang et al., 2010; Ghan et al., 2012; Yang et al., 2017a). Considering the lifetime of most aerosol particles and their locally uneven distribution, as well as their high dependence on emission sources and local meteorological conditions for dispersion (Rodwell and Jung, 2008; Liu et al., 2012; Liao et al, 2015), the impacts of episodic aerosol events over regional areas are worthy of more concerns (Cheng et al., 2017; Zheng et al., 2019).

With substantial aerosol loading, aerosol particles have significant influences on meteorology, and many endeavors by both field experiments and numerical models have been devoted to study the impacts of aerosol-radiation interaction on meteorological fields, including surface solar radiation, planetary boundary layer (PBL), atmospheric heating rate, atmospheric stability (Hansen et al., 1997; Ackerman et al., 2000; Quan et al., 2014; Yang et al., 2017b; Wang et al., 2018), cloud formation due to thermodynamic changes, and further the onset or reduction of precipitation

88   systems (Grell et al., 2011; Guo et al., 2016, Jiang et al., 2017). For instance, in

89   worldwide, the simulations with Weather Research and Forecasting (WRF) model

90   coupled with Chemistry (WRF-Chem) showed that by purely taking into account the

91   aerosol-radiation interactions, aerosols may reduce incoming solar radiation by up to

92   –9% (–16%) and 2-m temperatures by up to 0.16°C (0.37°C) in January (July) over

93   the continental U.S. (Zhang et al., 2010) , affect meso-scale convection system owing

94   to thermodynamic changes over Atlantic Ocean during Saharan dust eruption period

95   (Chen et al., 2017), and lead to the distinct changes in precipitation due to the changes

96   in temperature profile and stabilities induced by the aerosol-radiation interaction over

97   Eastern China (Huang et al., 2016).

98   Northern China is experiencing heavy air pollution in past two decades, with

99   particle matter (PM) being the primary pollutant, particularly during wintertime (Chan

100 and Yao, 2008; Zhang et al., 2015; Zhao et al., 2019) due to the combination of high

101 primary and precursor emissions and frequent stable meteorological conditions in this

102 area (Elser et al., 2016; Zhang et al, 2018). The effects of aerosol-radiation interaction

103 on meteorology were expected to be much more significant over northern China.

104 Applying WRF and Community Multi-scale Air Quality Model (CMAQ) system

105 (WRF-CMAQ), Wang et al. (2014) and Sekiguchi et al. (2018) reported a 53%

106 reduction in solar radiation reaching surface and ~100m decrease of planetary

107 boundary layer height (PBLH) in response to the presence of aerosols during a severe

108 winter haze episode in China. Wang et al. (2015a, b) used the online chemical weather

109   forecasting mode Global/Regional Assimilation and PrEdiction System/ Chinese

110   Unified Atmospheric Chemistry Environment (GRAPES/CUACE) and illustrated that

111   the solar radiation at ground decreased by 15% in Beijing–TianJin–Hebei, China, and

112   its near surroundings, accompanied by the decrease in turbulence diffusion of about

113   52% and a decrease in PBLH of about 33 % during a haze episode of summertime in

114   2008.

115   Considering the significant influence of the aerosol-radiation interaction on

116   meteorological forecasts as illustrated in many studies (Kaufman et al., 2002; Zhang

117   et al., 2010), several weather forecast centers are conducting research to facilitate the

118   inclusion of more complex aerosol information in operational numerical weather

119   prediction (NWP) models. For example, Rodwell and Jung (2008) showed the local

120   medium-range forecast skills were improved due to the application of new

121   climatological aerosol distribution in European Centre for Medium-Range Weather

122   Forecasts (ECMWF). Recently, a positive impact up to a 48h lead time on the 2m

123   temperature and forecasts of surface radiative fluxes were reported in ECMWF by

124   applying the prognostic aerosols compared to the monthly climatological aerosol

125   (Rémy et al., 2015). Toll et al. (2016) found that the inclusion of aerosol effects in

126   NWP system was beneficial to the accuracy of simulated radiative fluxes, temperature

127   and humidity in the lower troposphere over Europe. In addition, it was shown that the

128   quality of weather forecasts at UK MET office can be further advanced when the

129   real-time aerosol distribution rather than climatological distribution was included,

130   with the decreased bias of downward SW at surface (-2.79 W m^{-2} vs. -5.30 W m^{-2})

131   and the mean sea-level pressure (0.71hPa vs. 0.80hPa) (Mulcahy et al., 2014; Toll et

132   al., 2015). For these research serving for operational NWP systems, both online and

133   offline approaches (that aerosol information were simulated by separate chemistry

134   system and then offline coupled to NWP model) were widely used.

135   In most previous research-targeted modeling studies over northern China, the

136   aerosol-radiation interaction has been widely assessedin online-coupled

137   meteorology-chemistry models, which might not be practical for NWP purpose.

138   Considering aerosol particles differ by morphology, size and chemical composition,

139   therefore, the numerical treatment of aerosol particles in atmospheric models needs

140   sophisticated method and considerable simplifications, which may bring in more

141   assumptions and uncertainties in online coupling (Baklanov et al., 2014). Moreover,

142   the online simulations require quite high computational costs and could not meet the

143   requirement of efficiency for operational NWP. Grell and Baklanov (2011) illustrated

144   that the offline approach could generate to almost identical results compared to online

145   simulation with the offline-coupling intervals about 0.5-1h. Thus, the

146   computational-economic offline simulation provides a feasible and computationally

147   less demanding approach to include the aerosol-radiation interaction in an operational

148   NWP system. Péré et al. (2011) adopted an offline-coupling between the

149   chemistry-transport model CHIMERE and WRF to study the radiative forcing of high

150   load aerosols during the heat wave of summer in 2003 over Western Europe. Wang et

151 al. (2018) offline implemented the daily AOD from Moderate Resolution Imaging

152 Spectroradiometer (MODIS) to WRF during a heavy winter pollution at Beijing to

153 study the effect of aerosols on boundary layer. Still, there have been few studies that

154 adopted offline simulation to investigate the impacts of aerosol-radiation interactions

155 over northern China in an NWP system. At Institute of Urban Meteorology, regional

156 operational NWP system–RMAPS-ST (adapted from WRF) and regional air quality

157 model–RMPSA-Chem (adapted from WRF-Chem) were applied operationally. In this

158 study, we investigate the radiative effects of aerosols and their feedbacks on weather

159 forecasting over northern China during a polluted event occurred in winter of 2015,

160 and further potential impacts of changed meteorology to the transport and dissipation

161 of pollution. The simulations were in the configurations of the two systems, aiming at

162 presenting the offline-coupling of the high-frequent real-time aerosol distribution

163 simulated by WRF-Chem and WRF, and evaluating the potential effects of

164 aerosol-radiation interactions on the forecast skills in the RMAPS-ST system for

165 future applications.

166   The remainder of the paper is organized as follows. Section 2 presents the model

167 configuration and experimental design. In section 3, the model's capabilities in

168 capturing and forecasting the pollution episode are validated with observations first,

169 and impacts of aerosol-radiation interactions on meteorological forecasting over

170 northern China are analyzed further. The final section provides the concluding

171 remarks.

172   **2. Model description and experimental design**

173   WRF is a state-of-the-art atmospheric modeling system designed for both

174   meteorological research and NWP. The WRF version 3.8.1 released in August, 2016

175   was used in this study for a domain covering the northern China with a horizontal

176   resolulation of 9km (222×201 grid points, Fig. 1a), and for 50 vertical levels. The

177   lateral boundary condications (BCs) and initial conditions (ICs) for meteorological

178   variables are provided by the forecast of ECMWF. The major physical schemes

179   include the Assymetric Convective Model Version 2 (ACM2) PBL scheme (Pleim,

180   2007), the Thompson microphysics without aerosol-aware option (Thompson et al.,

181   2008), the Kain-Fritsch cumulus parameterization (Kain, 2004), and the National

182   Center for Environmental Prediction, Oregon State University, Air Force, and

183   Hydrologic Research Lab's (NOAH) land-surface module (Chen and Dudhia, 2001;

184   Ek et al., 2003). The landuse data have been reprocessed, with a higher accuracy and

185   finer classification for urban areas (Zhang et al., 2013) and the urban canopy model

186   (UCM) was not actived.

187   The shortwave and longwave radiation scheme is the Rapid Radiative Transfer

188   Model for General Circulation Models (RRTMG) (Iacono et al., 2008). The RRTMG

189   scheme is a new version of RRTM added in Version 3.1, and includes the Monte

190   Carlo Independent Column Approximation (MCICA) method of random cloud

191   overlap. A recent intercomparison study showed that the RRTMG had relativlely

192   smaller mean errors in solar flux at the surface and the top of the atmosphere

193 (Oreopoulos et al., 2012) and was considered as recommended WRF configuration

194 for air quality modeling (Rogers et al., 2013). The RRTMG scheme is capable to

195 include the climatological aerosol data with spatial and temporal variations or an

196 external time varing 3D aerosol input through the option of AER_OPT (Ruiz-Arias

197 et al., 2014). In the present study, the real-time hourly aerosol optical depth (AOD)

198 at 550nm from external files was input into WRF following the second approach.

199 The AOD at 550nm was calculated as the vertical integral of extinction coefficients at

200 550nm from WRF-Chem simulation.

201   WRF-Chem version 3.3.1 was applied in this study, and the horizontal

202 resolution was 9 km, with 222×201 grid points covering northern China, which was

203 the same configurion of WRF mentioned above. WRF-Chem simulates the formation,

204 transformation and transport processes of both primary and secondary atmospheric

205 pollutants, including gases and PM species (Zhao et al., 2019). Physical

206 parameterizations included single-layer Urban Canopy Model, Noah land-surface,

207 Yonsei University (YSU) PBL, Grell-Devenyi ensemble convection, Thompson

208 microphysics, and RRTM longwave and Goddard shortwave radiation (Chen and

209 Dudhia, 2001; Hong et al., 2006; Grell and Dévényi, 2002; Thompson et al., 2008;

210 Mlawer et al., 1997; Chou and Suarez, 1999). Carbon bond mechanism Z (CBMZ)

211 including comprehensive reactions and alterable scenarios were used as the

212 gas-phase mechanism. Model for Simulating Aerosol Interactions and Chemistry

213 (MOSAIC) are used with four size bins (Zaveri and Peters, 1999). Anthropogenic

214   emission data were from the MEIC (2012) inventory (http://www.meicmodel.org/)

215   with a resolution of 0.1 °×0.1 °. Meteorological ICs and BCs were obtained from the

216   Final Analysis data (FNL) with a resolution of 1.0 °×1.0 ° from the National Centers

217   for Environmental Prediction (NCEP). To generate aerosol fields for study period

218   (Dec. 2nd-11th), 9-days WRF-Chem simulations from Dec. 2nd were conducted using

219   prescribed idealized profiles as ICs and BCs for chemical species.

220   To estimate the aerosol radiative forcing and its feedbacks on meteorological

221   fields, two sets of 24-hour WRF forecasts were conducted at 00UTC from 2nd-10th

222   December 2015. The only difference between the two sets of forecasts is whether the

223   aerosol radiative feedback is activated (Aero, with WRF-Chem simulated hourly

224   AOD fields as input fields) or not (NoAero, no aerosol included), and other schemes

225   remained the same. It is noted that the aerosol-cloud interactions were not included

226   in the study.

227   The sites of observations over simulated domain and northern China plain (NCP,

228   purple box in Fig. 1a) were shown in Fig. 1. The 550nm AOD retrievals from Level

229   2 of MODIS sensors onboard polar orbiting satellites Terra and Aqua satellites were

230   adopted to evaluate the spatial distribution of modeled AOD. The vertical

231   distribution of aerosol extinction coefficient at 550nm were compared with that from

232   Cloud-Aerosol Lidar and Infrared Pathfinder Satellite Observations (CALIPSO)

233   satellite. Moreover, three sites of AErosol Robotic NETwork (AERONET) were

234   used to validate the simulation (black dots in Fig. 1b), and the observed AOD

235 obtained from observation at the Institute of Atmospheric Physics (IAP), Chinese

236 Academy of Sciences (39°58′ 28″ N, 116°22′ 16″ E) in Beijing city (blue dot in

237 Fig. 1b) was also included as supplementary. The hourly observed $PM_{2.5}$

238 concentrations of total 813/332 monitoring stations over the study domain/NCP

239 were from the released data by the China National Environmental Monitoring Centre

240 (http://106.37.208.233:20035/, colored dots in Fig. 3a). For given cities (dots in Fig.

241 1a), hourly $PM_{2.5}$ concentration was represented by the average of data from all

242 monitoring sites located in the city. Simulated meteorological variables including

243 2-m temperature and wind speed at 10m were evaluated using in-situ observations

244 from   National   Meteorological   Information   Center

245 (http://data.cma.cn/data/cdcindex.html) of China Meteorological Administration

246 (CMA, dots in Fig. 8a). The radiations were observed at IAP and in-situ stations of

247 CMA (shown as triangles in Fig. 1a). The vertical observation of atmospheric wind

248 speed from sounding were also used (circles in Fig. 1a). The variables, sources,

249 numbers of sites in the domain and NCP and the frequency of chemical and

250 meteorological observations were also listed in Table 1.

251 **3. Results**

252 **3.1 Evaluation of AOD and $PM_{2.5}$ simulated by WRF-Chem**

253 Before the offline-coupling of the WRF-Chem simulated hourly AOD to

254 meteorological model WRF, we first validated the simulated AOD and ensured the

255 model's capability to reproduce the features of the aerosol field. Figure 2 shows the

256   spatial distribution of modeled AOD and AOD from MODIS Terra and Aqua. It was

257   seen that WRF-Chem is capable to capture the AOD spatial distribution and also

258   reproduced the transport paths during the event. The simulated high-valued AOD

259   located in Henan on Dec. 6th, then the center moved to Hebei and Beijing on 7th and

260   shifted to northeast areas afterwards. The variations of simulated AOD were in

261   consistent with both Terra and Aqua with slightly overestimated peak value of AOD.

262   In particular, the simulated shifting of AOD center to northeast areas was also

263   observed in Aqua (Fig. 2r-s). To further verify the vertical distribution of aerosol

264   extinction coefficient, Fig. 3 displayed the vertical distribution of simulated 550nm

265   aerosol extinction coefficient compared to those from CALIPSO. Four cross sections

266   along CALIPSO paths on 6th to 9th December were shown. The results indicated that

267   the model could generally reproduce the vertical distribution of extinction

268   coefficients at 550nm in terms of comparable magnitude with those from CALIPSO,

269   particularly on 6th, 7th and 9th, December. However, CALIPSO showed more high

270   values at lower altitude (below 1km) that model failed to capture; the inconsistency

271   may be associated with both CALIPSO retrieval uncertainties at the low altitude and

272   the model itself. Figure 4 further displayed the temporal variation of simulated AOD

273   at 550nm (blue solid) at four sites, in comparison with three AERONET stations

274   (black circles in Figs. 4a-c) and IAP site (black circles in Fig. 4d) for the period

275   during 3rd to 11th December, 2015 (local time, LT). As shown in blue solids in Fig.

276   4a, the simulated AOD increased since 6th Dec. and reached the peak value of 9 on

277   7th, and the high AOD value maintained until 9th and reached the second peak. The

278   second peak was also observed from AERONET though most of them were missing

279   during the pollution event. The temporal variations of AOD at Beijing-CMA and

280   IAP (Figs. 4b and d) were similar to those at Beijing station (Fig. 4a). Meanwhile,

281   the simulated AOD at Xianghe (Fig. 4c) was relatively lower than those at other

282   stations.

283   Considering that the aerosol extinction was mainly attributed to scattering and

284   absorption of solar radiation by $PM_{2.5}$ and their hygroscopic growth with relative

285   humidity (Cheng et al., 2006), next we compared the simulated $PM_{2.5}$ concentrations

286   with corresponding in-situ observation over the model domain. As shown in Fig. 5,

287   the simulated and observed pollution were both initiated over Henan province on 6th,

288   further intensified and shifted northward afterwards. The polluted center located

289   over south of Hebei province and maintained until 10th, with the maximum $PM_{2.5}$

290   concentration exceeding 440μg m^{-3}. The results indicated that WRF-Chem could

291   well capture the spatial features of $PM_{2.5}$ and its temporal variation, in spite of the

292   slight discrepancy of the center position during 9th and 10th. Figure 6 displayed the

293   mean bias, root mean square error (RMSE), and correlation coefficient during the

294   heavy pollution and relatively cleaner periods. It was seen that the biases of $PM_{2.5}$

295   were generally less than 40 μg m^{-3} with the correlation coefficient exceeding 0.8

296   during clean period (Fig. 6a-c). Compared with clean period, the bias and RMSE

297   were generally larger during polluted period (Fig. 6d-f). The $PM_{2.5}$ concentrations

298   over most areas of the domain were underestimated with the maximum bias

299   exceeding 160μg m^{-3}. Overall, the correlation coefficient was generally higher than

300   0.4 in northern China during the polluted period, particularly over Beijing with the

301   correlation coefficient reaching 0.8.

302   To further assess the temporal evolutions of the pollution, the simulated PM$_{2.5}$

303   concentrations at three major cities (Beijing, Shijiazhuang and Tianjin, shown as

304   black dots in Fig. 1a) and two provinces (Hebei and Henan) in northern China were

305   compared with observation as shown in Fig. 7. It showed that the hourly variations

306   of PM$_{2.5}$ concentration, including the occurrence of several high peaks at the three

307   cities, as well as the gradual accumulation of pollution in Hebei and Henan could be

308   reasonably reproduced by WRF-Chem. The correlation coefficients (R) between

309   simulation and observation at Beijing, Shijiazhuang, Tianjin, Hebei and Henan were

310   0.85, 0.89, 0.76, 0.92 and 0.77 respectively. It should be noted that there exits slight

311   overestimation (underestimation) of the peak magnitude during 9th to 10th at Beijing

312   and Shijiazhuang (Tianjin, Hebei and Henan); the overestimation in Beijing and

313   Shijiazhuang is possibly associated with the frequent emission changes caused by

314   emission-control-measures in reality which are not dynamically updated in the model;

315   the underestimation is more related with the deficiency of model skills, such as

316   missing heterogeneous reaction paths in the chemistry scheme.

317   **3.2 Aerosol effects on meteorological simulations**

318   In this section, the influences of aerosol-radiation interaction on the spatial and

319   temporal variations of radiation and energy budget simulated by WRF model were

320   analyzed, and their impacts on the forecasts of meteorological fields were discussed

321   further.

322   **3.2.1   Aerosol impacts on simulations of radiative forcing and heat fluxes**

323   To illustrate the impacts of aerosol-radiation interaction on the forecasts of

324   radiation during the pollution event, the simulated surface downward SW radiation

325   and net radiation at Beijing, Tianjin, Taiyuan and Jinan, as denoted by the triangles

326   in Fig. 1a, were compared with observations in Fig. 8. To show the relationship with

327   aerosol, the time series of AOD for Dec. 3th -11th were overlaid as gray shadings in

328   Fig. 8. During the clean stage with quite low AOD values (close to 0) before 6th Dec.,

329   both simulations with and without aerosols reasonably reproduced the temporal

330   variation of downward SW at Beijing despite the slightly overestimation during the

331   noon-time (Fig. 8a). However, the overestimated downward SW in NoAero turned

332   to intensify extensively since 6th Dec. and sustained till 10th Dec., accompanied by

333   the occurrence of the pollution with the high AOD value. Meanwhile, the downward

334   SW was much lower in Aero than that in NoAero due to aerosol extinction, with

335   resembled temporal variations and comparable magnitude at the peak time compared

336   to the observations. Similarly, the variations of downward SW from Aero simulation

337   were also closer to observations at Tianjin, Taiyuan and Jinan than those in NoAero

338   (Figs. 8b-d). It was noted that the most significant improvement of simulated

339   downward SW at Jinan appeared on 10th Dec. and was later than that at Beijing,

340   which was consistent with the AOD's variations at Jinan. Moreover, the surface

341   energy balance was also affected by the reduction of downward SW radiation

342   reaching the ground due to the presence of aerosol particles. As shown in Figs. 8e–h,

343   in corresponding to the changes in downward SW, the variations of net radiation at

344   surface in Aero were also in better agreement with observation during the polluted

345   period than in NoAero, particularly during daytime with the high AOD values.

346   To further quantify the influence of the aerosol-radiation interaction on the

347   diurnal variation of surface radiation, next we compared the simulated averaged

348   diurnal variation of downward SW and net radiation during the polluted episode (6th

349   to 10th) with observation. Figure 9a showed that there existed a large overestimation

350   of surface downward SW during the daytime in NoAero. Particularly, the

351   overestimated downward SW tented to increase since morning (0800 LT) and peak

352   at noon (1300 LT) with the maximum bias reaching 226.5 W m^{-2}, and the mean bias

353   of ~149.4 W m^{-2} during daytime (averaged during 0800 to 1800 LT, Table 2).

354   However, the overestimated SW radiation was remarkably reduced in Aero with the

355   mean bias of 38.0 W m^{-2} during daytime. Similarly, the diurnal variation and

356   magnitude of downward SW radiation at surface were also better captured at Tianjin,

357   Taiyuan and Jinan in Aero (Figs. 9b–d), with the lower bias (70.9 W m^{-2}, 118.3 W

358   m^{-2} and 97.7 W m^{-2}) than in NoAero (115.5 W m^{-2}, 155.0 W m^{-2} and 149.1 W m^{-2})

359   during daytime. Note the biases of SW radiation in Tianjin, Taiyuan and Jinan were

360   not improved as much as in Beijing due to the lower AOD. Consistent with this

361 finding, the reduction of downward SW was also reported in United States (Zhang et

362 al., 2010) and Europe (Toll et al., 2016) with relatively lower decrease (10 W m^{-2}

363 and 18 W m^{-2}); the relatively larger reductions (30-110 W m^{-2}) in northern China is

364 possibly due to the higher aerosol load. Figures 9e–h presented the diurnal variations

365 of net radiation, with positive (negative) net radiation during daytime (nighttime) in

366 observation, and the NoAero tended to overestimate (underestimate) the net

367 radiation at surface during daytime (nighttime), indicating that there existed surplus

368 energy income and outcome in model than those in observation, inducing the larger

369 magnitude of diurnal cycle of net radiation. By including the aerosol-radiation

370 interaction in the model, the simulated diurnal variations of net radiation were

371 markedly improved, particularly during daytime with the reduction of bias by 85.3%,

372 50.0%, 35.4%, and 44.1% at Beijing, Tianjin, Taiyuan and Jinan, respectively.

373   In response to the decrease of downward SW radiation and net radiation at the

374 ground during daytime, the surface fluxes also changed in presence of aerosol

375 extinction within the energy-balanced system. Figure 10 displayed the difference of

376 surface sensible and latent heat flux between Aero and NoAero at 1300LT, when the

377 influences of the aerosol on radiation reaching the peak. Comparing to the NoAero

378 simulation, both the surface sensible and latent heat flux emitted by the surface were

379 reduced in the Aero simulation, with the domain-average of 16.1 W m^{-2} (18.5%) and

380 6.8 W m^{-2} (13.4%) respectively. It was noted that the decrease of the surface latent

381 heat flux was less pronounced than that of surface sensible heat flux, suggesting the

382   impact of aerosol-radiation interaction on the humidity was less significant than that

383   of temperature, which was also reported over United States (Fan et al., 2008) and

384   western Europe (Péré et al., 2011).

385   **3.2.2   Aerosol impacts on simulations of temperature, PBLH and wind fields**

386   The changes in radiation and energy budget through the impacts of

387   aerosol-radiation interaction would certainly induce the changes in PBL

388   thermodynamics and dynamics, which would result in changes in the forecasts of

389   meteorological fields. The impacts on the forecasts of 2-m temperature, PBLH and

390   wind fields due to the aerosol-radiation interaction are discussed in the following

391   subsection.

392   Figure 11 presented the diurnal variation of averaged bias of 2-m temperature

393   during polluted period in NoAero (upper panel) and Aero (lower panel) compared

394   with the in-situ observation during 1100 LT to 2300 LT. It was obvious that the

395   temperature of NoAero was significantly overestimated for a wide range over

396   northern China, particularly over the plain areas including south of Hebei, Henan

397   and Shanxi provinces. The warm biases tended to intensify in the afternoon and

398   reach ~3°C over south part of Hebei province (Figs. 11b–c). Accompanied by the

399   warm biased over plain areas throughout the day, the mountain areas were

400   dominated by the cold biases until 1700 LT, and turned to be warm biases afterwards,

401   which were attributed by the frozen water in soil due to wet bias of soil moisture

402   over mountain areas, inducing overestimated energy transport from atmosphere to

403   soil during daytime. Compared to NoAero, the lower temperature in Aero due to the

404   decreased surface solar radiation, caused by aerosol extinction led to the reduced

405   warm bias in NCP region. However, the cold bias in Beijing area was slightly

406   intensified, which may partly relevant with the overestimated $PM_{2.5}$ concentration in

407   Beijing and can be improved by incorporating more accurate aerosol information in

408   the future. It was noted that the cold biases over mountain areas associated with the

409   model physics deficiency can not be corrected by aerosol-radiation effects, thus the

410   correction of aerosol-radiation effect may get complex results and differ with

411   regions due to the model pre-existing deficiencies.

412   To quantitatively evaluate the agreement of simulated 2-m temperature with

413   observations, the mean bias and RMSE were employed, and their averaged diurnal

414   variations during the polluted episode (6th to 10th, Dec.) averaged over NCP, denoted

415   by the purple box in Fig. 1a, were displayed in Fig. 12. As shown in Fig. 12a, the

416   warm bias in NoAero sustained during the entire 24-hr forecast, ranging from 0.3 °C

417   to 0.9 °C. Compared to NoAero, the NCP area-averaged warm bias was remarkably

418   reduced by ~0.40°C (~73.9%) due to aerosol-radiation interaction, with the

419   maximum reaching ~0.54 °C (~95.0 %) at 1100 LT (Figs. 12a and c). Consistently

420   with mean bias, the RMSE was also lower in Aero than NoAero, particularly during

421   1100 to 2000 LT during the daytime (Figs. 12b and d).

422   The aerosol-radiation interaction may also have profound impacts on atmospheric

423   structure in addition to radiation and temperature (Rémy et al., 2015). PBLH is one

424   of the key parameters to describe the structure of PBL and closely related to air

425   pollution. It was indicated that the mean daytime PBLH over northern China were

426   around 300–600m (Fig. 13a), and declined generally 40–200m (10%–40%) in Aero

427   over the region with highest $PM_{2.5}$ concentration, particularly over Beijing, Tianjin

428   and Hebei (Figs. 13b–c). As shown in dashed lines in Fig. 14, the NCP

429   area-averaged PBLH at noon-time (1400 LT) was diminished dramatically by

430   aerosol-radiation interaction during the pollution event over northern China, with the

431   maximum decrease reaching -155.2m on 7th Dec. The reduction of PBLH could be

432   the consequence of more stable atmosphere in Aero than NoAero, which was

433   induced by the terrestrial cooling in the lower part of the planetary boundary layer

434   and the solar heat due to the absorbing in the upper layers (solid lines in Fig. 14).

435   The near surface wind fields changes due to aerosol-radiation interaction were

436   further investigated. Figure 15 shows the wind vector in NoAero (upper panel), Aero

437   (middle panel) and their difference (lower panel). It can be seen from Fig. 15a-e that

438   the northern China was dominated by the anticyclonic circulation, accompanied by

439   the relatively weaker northeast wind over Beijing and Hebei areas. The comparisons

440   of Aero and NoAero (Figs. 15 k-o) showed that the northeast wind was increased

441   with the maximum reaching 1 m s $^{-1}$ by aerosol-radiation interaction over Beijing

442   and Hebei, where high particles concentration located (shadings in Figs. 15 f-j).

443   Figures 15k-o also indicated the changes of west wind over the south part of the

444   domain and southeast wind over the ocean areas, which tended to weaken the

445   anticyclonic circulation and thus declined the wind speed there. The reduced wind

446   speed due the inclusion of aerosol-radiation interaction was possible due to the

447   thermal-wind adjustment in response to the more stable near-surface atmosphere,

448   which was also addressed in previous work using WRF-Chem (Zhang et al., 2015).

449   The comparisons between simulated wind speeds against in-situ observation

450   averaged during 6th to 10th Dec. were displayed in Fig. 16. In regard of NoAero, the

451   simulated wind speed at 10m was overestimated over the nearly whole domain with

452   the maximum bias up to 3 m s^{-1} except some mountain sites (upper and middle

453   panels in Fig.16). It might be due to the omission of UCM model as the

454   overestimation is more prominent in city clusters (especially in Beijing and southern

455   Hebei) than other areas. Figures 16k-o showed the difference of absolute value of

456   bias between Aero and NoAero and indicated the bias of simulated wind speed were

457   decreased over south and northeast part of the domain during afternoon (Figs. 16k-m)

458   by aerosol-radiation interaction, while were increased over Beijing and Hebei area

459   particularly during nightfall (Fig. 16n) due to the intensified wind speed there. The

460   NCP area-averaged bias and RMSE of wind speed at 10m were further shown in

461   Figure 17. It was seen that the aerosol-radiation interaction helped to reduce the

462   overestimation of wind speed at 10m up to 0.08 m s^{-1} (~7.8%), particular during

463   daytime (Figs. 17a and c). Correspondingly, the RMSE of Aero was also lower than

464   that of NoAero, indicating that the inclusion of aerosol-radiation interaction helped

465   to improve the prediction of near surface wind speed on the domain-averaged scale.

466   Although the changes of wind speed are less straightforward than that of radiation,

467   the aerosol-radiation interactions can also affect dynamic fields (vertical wind shear)

468   through the changes of atmospheric thermal structure and the thermal wind relation

469   when the interaction lasts long enough (Huang et al., 2019). Figure 18 displayed

470   vertical profiles of wind speed at the stations of Beijing and Xingtai in simulation

471   and verified with sounding observations. It was shown that the NoAero

472   underestimated (overestimated) the low levels wind speed at 0800 LT (2000 LT) at

473   both Beijing and Xingtai. However, the wind speed was increased (decreased) at

474   0800 LT (2000 LT) in Aero relative to NoAero, indicating the positive impacts on

475   the simulation of atmospheric winds by aerosol-radiation interaction.

476   Since the forecast meteorological fields by WRF (RMPAS-ST) is routinely

477   applied to WRF-Chem (RMAPS-Chem) as meteorological ICs in the air quality

478   operational system at IUM, the changed meteorology due to aerosol-radiation

479   interaction will further influence the forecast of pollution through meteorological

480   ICs. In regard of further feedback of aerosol-radiation interactions to the transport

481   and dissipation of the pollutants, their impacts on wind field at 850hPa were further

482   discussed as it is strongly correlated with haze formation (Zhang et al., 2018; Zhai et

483   al., 2019). Figures 19 a-e display that northern China was dominated by the

484   anticyclone circulation at 850hPa, associated with the southwest (northwest) wind in

485   the west (east) of the northern part of the domain. The difference of U (zonal,

486   eastward is positive) winds between Aero and NoAero (middle panel in Fig. 16)

487   showed that the U wind was intensified over west Hebei, accompanied by the quite

488   small changes in Beijing area, indicating that the increased U wind was blocked by

489   the mountains and could not transport the pollutants over Hebei and Beijing to the

490   east (Figs. 19 f-h). On the other hand, the changes of V (meridional, northward is

491   positive) show different patterns over north and south of the 38° N (lower panel in

492   Fig. 19). In the south part, the increased northward wind due to aerosol-radiation

493   interaction may help to transport pollutants from highly polluted areas to Hebei and

494   Beijing. In the north of the domain, the negative (positive) changes of V wind

495   indicated the reduced northward (southward) wind in west (east) of Hebei, which

496   could suppress the diffusion of the pollutants. As a result, both U and V changes

497   induced by the aerosol-radiation interaction will prevent pollutants from dispersing

498   and may exacerbate the pollution in Heibei and Beijing, which confirms the more

499   stable boundary layer due to aerosol-radiation interaction as discussed earlier.

500   **4. Concluding remarks**

501   To facilitate the future inclusion of aerosol-radiation interactions in the regional

502   operational NWP system – RMAPS-ST (adapted from WRF) at IUM, CMA, the

503   impacts of aerosol-radiation interactions on the forecast of surface radiation and

504   meteorological parameters during a heavy pollution event (Dec. 6th -10th, 2015) over

505   northern China were investigated. The aerosol information (550-nm AOD 2D field)

506   were simulated by WRF-Chem and then offline-coupled into RRTMG radiation

507   scheme of WRF to enable the aerosol-radiation feedback in the forecast. Two sets of

508 24-hour forecasts were performed at 00UTC from Dec. 2nd-11th, 2015. The only

509 difference between the two sets of forecasts was whether the aerosol radiative

510 feedback was activated (Aero, with WRF-Chem simulated hourly AOD fields as

511 input fields) or not (NoAero, no aerosol included), while the other schemes

512 remained the same.

513 The capability of WRF-chem to reproduce the polluted episode was confirmed

514 first before the offline-coupling of AOD to WRF. The validation of simulated AOD

515 and aerosol extinction coefficient against MODIS and CALIPSO confirmed that the

516 model could reproduce both the spatial and vertical distribution of 550nm AOD.

517 Further results indicated that the temporal variations of simulated AOD at 550nm

518 was in consistent with AERONET and in-situ observation at IAP. In addition, the

519 spatial distributions of PM$_{2.5}$ as well as their magnitude, particularly during the peak

520 stage (8th to 9th) of the pollution event were reasonably captured by WRF-Chem,

521 with the correlation coefficients of 0.85, 0.89, 0.76, 0.92 and 0.77 at Beijing,

522 Shijiazhuang, Tianjin, Hebei and Henan, respectively.

523 Further, the impacts of aerosols-radiation interaction on the forecasts of surface

524 radiation, energy budget, and meteorology parameters were evaluated against

525 surface and sounding observations. The results showed that the decrease of

526 downward SW radiation reaching surface induced by aerosol effects helped to

527 reduce the overestimation of SW radiation during daytime. Moreover, the simulated

528 surface radiation budget has also been improved, with the biases of net radiation at

529   surface decreased by 85.3%, 50.0%, 35.4%, and 44.1% during daytime at Beijing,

530   Tianjin, Taiyuan and Jinan respectively, accompanied by the reduction of sensible

531   (16.1 W m^{-2}, 18.5%) and latent (6.8 W m^{-2}, 13.4%) heat fluxes emitted by the

532   surface at noon-time.

533   The energy budget changed by aerosol extinction further cools 2-m temperature

534   by ~0.40°C over NCP, reducing warm bias by ~73.9% and also leading to lower

535   RMSE, particularly during daytime. Since aerosol cools the lower planetary

536   boundary layer and meanwhile warms the high atmosphere, it induced the more

537   stable stratification of the atmosphere and the declination of PBLH by 40–200m

538   (10%–40%) over NCP. Associating with the changes of planetary boundary structure

539   and more stable near-surface atmosphere, the aerosol-radiation interaction tended to

540   weaken the anticyclonic circulation including the east wind over the south part of

541   the domain and northwest wind over the ocean areas. Thus the bias of wind speed

542   over south and northeast part of the domain were decreased particularly during the

543   afternoon, while increased over Beijing and Hebei area. In regard of NCP-average,

544   the overestimated 10m wind speed was improved during whole day with the

545   maximum up to 0.08 m s^{-1} (~7.8%) at 1400LT. The comparison between simulated

546   vertical profiles of atmospheric wind speed with soundings also indicated that Aero

547   was in better agreement with observation and aerosol-radiation interaction helped to

548   improve the prediction of dynamic fields such as atmospheric wind through the

549   thermal wind relation by altering the atmospheric structure.

550   The impacts of aerosol-radiation interactions on wind field at 850hPa were

551   further discussed. The results showed that aerosol-radiation interaction will prevent

552   pollutants from dispersing and may exacerbate the pollution through changes of both

553   U and V wind, which confirms the more stable boundary layer due to

554   aerosol-radiation. These wind field changes may also influence the forecast of the

555   transport and dissipation of the pollutants by WRF-Chem through changed

556   meteorological ICs.

557   This study analyzed the impacts of aerosol-radiation interaction on radiation and

558   meteorological forecast by using the offline-coupling of WRF and high-frequent

559   updated AOD simulated by WRF-Chem, which is more computationally economic

560   than the online simulation with the integration time for 96h forecast of about 40% of

561   that for online simulation. This approach allows for a potential application to include

562   aerosol-radiation interaction in our current operational NWP systems. The results

563   revealed that aerosol-radiation interaction had profound influence on the

564   improvement of predictive accuracy and the potential prospects for its application in

565   regional NWP in northern China. To verify the statistically significance of the

566   results, we further conducted the 24-hour forecasts for a longer period lasting 27

567   days (Jan. 13th – Feb. 8th, 2017), with no AOD field (NoAero) and WRF-Chem

568   simulated hourly AOD fields (Aero) included, as well as constant AOD value of

569   0.12 (ClimAero), respectively. The results showed that the mean RMSE of 2-m

570   temperature (wind speed at 10m) in Aero and ClimAero relative to NoAero was

571   reduced by 3.95% (1.86%) and 1.23% (1.63%), respectively (not shown). The

572   one-month results indicated that the simulation with the inclusion of WRF-Chem

573   simulated hourly AOD fields outperformed other two simulations and showed more

574   improvement on the meteorological forecast than the simulation with climatological

575   AOD fields. More detailed evaluations and analysis will be addressed in a future

576   article. As the simulated AOD was adopted in the present study, it should be noted

577   that there exits a discrepancy between simulated AOD and observation in both

578   spatial distribution and temporal variation, which may influence the impacts of

579   aerosol-radiation interaction. Meanwhile, surface energy budget and atmospheric

580   dynamics are also influenced by aerosol-cloud interaction, which are related to cloud

581   microphysical processes and are not discussed in this study.

582   *Data availability* Data are available upon request from the first authors Yang Yang

583   (yyang@ium.cn) and corresponding authors Xiujuan Zhao (xjzhao@ium.cn) and Dan

584   Chen (dchen@ium.cn).

585

586   *Author contribution* Yang Yang, Min Chen, Xiujuan Zhao and Dan Chen designed the

587   experiments, Yang Yang and Xiujuan Zhao performed the simulations and carried them

588   out. Yang Yang and Dan Chen prepared the manuscript with contributions from all

589   co-authors.

590

591   *Competing interests* The authors declare that they have no conflict of interest.

592

593   *Acknowledgments* This work was jointly supported by the National Key R&D

594   Program of China (grant nos. 2017YFC1501406 and 2018YFF0300102), Natural

595   Science Foundation of Beijing Municipality (8161004), the National Natural Science

596   Foundation of China (grant nos. 41705076, 41705087 and 41705135),

597   Beijing Major Science and Technology Project (Z181100005418014)   and   Beijing

598   Natural Science Foundation (grant no. 8204074).

599

600 **Reference**

601 Ackerman, A. S., Toon, O. B., Stevens, D. E., Heymsfield, A. J., Ramanathan, V.,

602   and Welton, E. J.: Reduction of tropical cloudiness by soot, Science, 288, 1042–

603   1047, https://doi.org/10.1126/science.288.5468.1042, 2000.

604 Baklanov, A., Schlünzen, K., Suppan, P., Baldasano, J., Brunner, D., Aksoyoglu, S.,

605   Carmichael, G., Douros, J., Flemming, J., Forkel, R., Galmarini, S., Gauss, M.,

606   Grell, G., Hirtl, M., Joffre, S., Jorba, O., Kaas, E., Kaasik, M., Kallos, G., Kong,

607   X., Korsholm, U., Kurganskiy, A., Kushta, J., Lohmann, U., Mahura, A.,

608   Manders-Groot, A., Maurizi, A., Moussiopoulos, N., Rao, S. T., Savage, N.,

609   Seigneur, C., Sokhi, R. S., Solazzo, E., Solomos, S., Sørensen, B., Tsegas, G.,

610   Vignati, E., Vogel, B., and Zhang, Y.: Online coupled regional meteorology

611   chemistry models in Europe: current status and prospects, Atmos. Chem. Phys.,

612   14, 317–398, https://doi.org/10.5194/acp-14-317-2014, 2014.

613 Chan, C. K. and Yao, X.: Air pollution in mega cities in China, Atmos. Environ., 42,

614   1–42, https://doi.org/10.1016/j.atmosenv.2007.09.003, 2008.

615 Chen, D., Liu, Z., Davis, C., and Gu, Y.: Dust radiative effects on atmospheric

616   thermodynamics and tropical cyclogenesis over the Atlantic Ocean using

617   WRF-Chem coupled with an AOD data assimilation system, Atmos. Chem. Phys.,

618   17, 7917–7939, https://doi.org/10.5194/acp-17-7917-2017, 2017.

619 Chen, F. and Dudhia, J.: Coupling an advanced land surface-hydrology model with

620   the Penn State-NCAR MM5 modeling system. Part I: Model implementation and

621   sensitivity, Mon. Wea. Rev., 129, 569–585, doi:

622   10.1175/1520-0493(2001)129<0569:CAALSH>2.0.CO;2, 2001.

623 Cheng, X., Sun, Z., Li, D., Xu, X., Jia, M., and Cheng, S.: Short-term aerosol

624   radiative effects and their regional difference during heavy haze episodes in

625   January 2013 in China, Atmos. Environ., 165, 248–263,

626   http://dx.doi.org/10.1016/j.atmosenv.2017.06.040, 2017.

627 Cheng, Y. F., Eichler, H., Wiedensohler, A., Heintzenberg, J., Zhang, Y. H., Hu, M.,

628   Herrmann, H., Zeng, L.M., Liu, S., Gnauk, T., Brüggemann, E., and He, L.Y.,

629   Mixing state of elemental carbon and non-light-absorbing aerosol components

630   derived from in situ particle optical properties at Xinken in Pearl River Delta of

631   China, J. Geophys. Res.-Atmos.,111, D20204, doi: 10.1029/2005JD006929,

632   2006.

633 Chou, M. D. and Suarez, M. J.: A solar radiation parameterization for atmospheric

634   studies, Tech. Rep. NASA/TM-1999-104606, 15, Technical Report Series on

635   Global Modeling and Data Assimilation NASA, 1999.

636 Ek, M. B., Mitchell, K. E., Lin, Y., Rogers, E., Grunmann, P., Koren, V., Gayno, G.,

637   and Tarpley, J.D.: Implementation of Noah land surface model advances in the

638   National Centers for Environmental Prediction operational mesoscale Eta model,

639   J. Geophys. Res.-Atmos, 108, 8851, doi:10.1029/2002JD003296, 2003.

640 Elser, M., Huang, R.-J., Wolf, R., Slowik, J. G., Wang, Q., Canonaco, F., Li, G.,

641   Bozzetti, C., Daellenbach, K. R., Huang, Y., Zhang, R., Li, Z., Cao, J.,

642   Baltensperger, U., El-Haddad, I., and Prévôt, A. S. H.: New insights into $PM_{2.5}$

643   chemical composition and sources in two major cities in China during extreme

644   haze events using aerosol mass spectrometry, Atmos. Chem. Phys., 16, 3207–

645   3225, https://doi.org/10.5194/acp-16-3207-2016, 2016.

646   Fan, J., Zhang, R., Tao, W. K., and Mhor, K. I.: Effects of aerosol optical properties

647   on deep convective clouds and radiative forcing, J. Geophys. Res., 113, D08209,

648   doi:10.1029/2007JD009257, 2008.

649   Ghan, S. J., Liu, X., Easter, R. C., Zaveri, R., Rasch, P. J., Yoon, J.-H., Eaton, B.:

650   Toward a Minimal Representation of Aerosols in Climate Models: Comparative

651   Decomposition of Aerosol Direct, Semidirect, and Indirect Radiative Forcing, J.

652   Clim., 2012, 25, 6461-6476, doi: 10.1175/JCLI-D-11-00650.1, 2012.

653   Grell, G. A. and Baklanov, A.: Integrated modelling for forecasting weather and air

654   quality: a call for fully coupled approaches, Atmos. Environ., 45, 6845–6851,

655   https://doi.org/10.1016/j.atmosenv.2011.01.017, 2011.

656   Grell, G. A. and Dévényi, D.: A generalized approach to parameterizing convection

657   combining ensemble and data assimilation techniques, Geophys. Res. Lett., 29,

658   1693, doi: 10.1029/2002GL015311, 2002.

659   Grell, G., Freitas, S. R., Stuefer, M., and Fast, J.: Inclusion of biomass burning in

660   WRF-Chem: impact of wildfires on weather forecasts, Atmos. Chem. Phys., 11,

661   5289-5303, https://doi.org/10.5194/acp-11-5289-2011, 2011.

662   Guo, J., Deng, M., Lee, S. S., Wang, F., Li, Z., Zhai, P., Liu, H., Lv, W., Yao, W., and

663   Li, X.,: Delaying precipitation and lightning by air pollution over the pearl river

664   delta. Part I: observational analyses, J. Geophys. Res.-Atmos, 121, 6472–6488,

665   doi:10.1002/2015JD023257, 2016.

666   Hansen, J., Sato, M., and Ruedy, R.: Radiative forcing and climate response, J.

667   Geophys. Res.-Atmos, 102, 6831–6864, https://doi.org/10.1029/96JD03436,

668   1997.

669   Hong, S.-Y., Noh, Y., and Dudhia, J.: A new vertical diffusion package with an

670   explicit treatment of entrainment processes, Mon. Weather Rev., 134, 2318–2341,

671   doi:10.1175/Mwr3199.1, 2006.

672   Huang, C.-C., Chen, S.-H., Lin, Y.-C., Earl, K., Matsui, T., Lee, H.-H., Tsai, I-C.,

673   Chen, J.-P., and Cheng, C.-T.: Impacts of Dust–Radiation versus Dust–Cloud

674   Interactions on the Development of a Modeled Mesoscale Convective System

675   over North Africa, Mon. Weather Rev., 47, 3301-3326.

676   https://doi.org/10.1175/MWR-D-18-0459.1, 2019.

677   Huang, X., Ding, A., Liu, L., Liu, Q., Ding, K., Niu, X., Nie, W., Xu, Z., Chi, X.,

678   Wang, M., Sun, J., Guo, W., and Fu, C.: Effects of aerosol–radiation interaction

679   on precipitation during biomass-burning season in East China, Atmos. Chem.

680   Phys., 16, 10063－10082, https://doi.org/10.5194/acp-16-10063-2016, 2016.

681   Iacono, M. J., Delamere, J. S., Mlawer, E. J., Shephard, M. W., Clough, S. A.,

682   Collins, W. D.: Radiative forcing by long-lived greenhouse gases: Calculations

683   with the AER radiative transfer models, J. Geophys. Res.-Atmos,113, D13, doi:

684   10.1029/2008JD009944, 2008.

685   Jiang, M., Feng, J., Li, Z., Sun, R., Hou, Y.-T., Zhu, Y., Wan, B., Guo, J., and Cribb,

686   M.: Potential influences of neglecting aerosol effects on the NCEP GFS

687   precipitation forecast, Atmos. Chem. Phys., 17, 13967–13982,

688   https://doi.org/10.5194/acp-17-13967-2017, 2017.

689   Kain, J. S.: The Kain-Fritsch convective parameterization: An update, J. Appl.

690   Meteorol., 43, 170–181, 2004.

691   Kaufman, Y. J., Tanre, D., and Boucher, O.: A satellite view of aerosols in the

692   climate system, Nature, 419, 215-223, http://dx.doi.org/10.1038/nature01091,

693   2002.

694   Liao, H., Chen, W. T., and Seinfeld, J. H.: Role of climate change in global

695   predictions of future tropospheric ozone and aerosols, J. Geophys. Res., 111,

696   D12304, doi:10.1029/2005JD006852, 2006.

697   Liao, L., Lou, S. J., Fu, Y., Chang, W. J., and Liao, H.: Radiative forcing of aerosols

698   andits impact on surface air temperature on the synoptic scale in eastern China,

699   Chinese J. Atmos. Sci. (in Chinese), 39, 68–82.,doi: doi:

700   10.3878/j.issn.1006-9895.1402.13302, 2015.

701   Liu, X., Zhang, Y., Cheng, Y., Hu, M., and Han, T.: Aerosol hygroscopicity and its

702   impact on atmospheric visibility and radiative forcing in Guangzhou during the

703   2006 PRIDE-PRD campaign, Atmos. Environ. 60, 59–67,

704   https://doi.org/10.1016/j.atmosenv.2012.06.016, 2012.

705   Mlawer, E. J., Taubman, S. J., Brown, P. D., Iacono, M. J. and Clough, S. A.:

706   Radiative transfer for inhomogeneous atmospheres: RRTM, a validated

707   correlated-k model for the longwave, J. Geophys. Res., 102,

708   doi:10.1029/97JD00237. 16663-16682, 1997.

709   Mulcahy, J. P., Walters, D. N., Bellouin, N., and Milton, S. F.: Impacts of increasing

710   the aerosol complexity in the Met Office global numerical weather prediction

711   model, Atmos. Chem. Phys., 14, 4749–4778,

712   https://doi.org/10.5194/acp-14-4749-2014, 2014.

713   Oreopoulos, L., Mlawer, E., Delamere, J., Shippert, T., Cole, J., Fomin, B., Iacono,

714   M., Jin, Z., Li, J., Manners, J., Räisä-nen, P., Rose, F., Zhang, Y., Wilson, M. J.,

715   and Rossow, W. B.: The Continual Intercomparison of Radiation Codes: Results

716   from Phase I, J. Geophys. Res.-Atmos., 117, D06118,

717   https://doi.org/10.1029/2011JD016821, 2012.

718   Péré, J. C., Mallet, M., Pont, V., and Bessagnet B.: Impact of aerosol direct radiative

719   forcing on the radiative budget, surface heat fluxes, and atmospheric dynamics

720   during the heat wave of summer 2003 over western Europe: A modeling study, J.

721   Geophys. Res., 116, D23119, https://doi.org/10.1029/2011JD016240, 2011.

722   Pleim. J. E.: A Combined local and nonlocal closure model for the atmospheric

723   boundary layer. Part I: Model description and testing, J. Appl. Meteorol. Climat.,

724   46, 1383–1395, doi: 10.1175/JAM2539.1, 2007.

725   Quan, J., Tie, X., Zhang, Q., Liu, Q., Li, X., Gao, Y., and Zhao D.: (2014).

726   Characteristics of heavy aerosol pollution during the 2012–2013 winter in beijing,

727   China, Atmos. Environ., 88, 83-89,

728   https://doi.org/10.1016/j.atmosenv.2014.01.058, 2014.

729   Ramanathan, V., Crutzen, P. J., Kiehl, J. T., and Rosenfeld, D.: Aerosols, Climate

730   and the Hydrological Cycle, Science, 294, 2119–2124, 2001.

731   Rémy, S., Benedetti, A., Bozzo, A., Haiden, T., Jones, L., Razinger, M., Flemming,

732   J., Engelen, R. J., Peuch, V. H., and Thepaut, J. N.: Feedbacks of dust and

733   boundary layer meteorology during a dust storm in the eastern Mediterranean,

734   Atmos. Chem. Phys., 15, 12909–12933,

735   https://doi.org/10.5194/acp-15-12909-2015, 2015.

736   Rodwell, M. J. and Jung T.: Understanding the local and global impacts of model

737   physics changes: an aerosol example, Q. J. Roy. Meteor. Soc., 134, 1479-1497,

738   https://doi.org/10.1002/qj.298, 2008.

739   Rogers, R. E., Deng, A. J., Stauffer, D. R., Gaudet, B. J., Jia, Y. Q., Soong, S. T., and

740   Tanrikulu, S.: Application of the Weather Research and Forecasting Model for Air

741   Quality Modeling in the San Francisco Bay Area, J. Appl. Meteor. Clim., 52,

742   1953–1973, doi: 10.1175/JAMC-D-12-0280.1, 2013.

743   Ruiz-Arias, J. A., Dudhia, J., and Gueymard, C. A.: A simple parameterization of the

744   short-wave aerosol optical properties for surface direct and diffuse irradiances

745   assessment in a numerical weather model, Geosci. Model Dev., 7, 1159–1174,

746   doi:10.5194/gmd-7-1159-2014, 2014.

747 Sekiguchi, A., Shimadera, H., and Kondo, A.: 2018, Impact of Aerosol Direct Effect

748   on Wintertime $PM_{2.5}$ Simulated by an Online Coupled Meteorology-Air Quality

749   Model over East Asia, Aerosol and Air Quality Research, 18: 1068–1079, doi:

750   10.4209/aaqr.2016.06.0282, 2018.

751 Thompson, G., Field, P. R., Rasmussen, R. M., and Hall, W. D.: Explicit forecasts of

752   winter precipitation using an improved bulk microphysics scheme. Part II:

753   Implementation of a new snow parameterization, Mon. Weather Rev., 136, 5095–

754   5115, https://doi.org/10.1175/2008MWR2387.1, 2008.

755 Toll, V., Gleeson, E., Nielsen, K.P., Männik, A., Mašek, J., Rontu, L., and Post, P.:

756   Impacts of the direct radiative effect of aerosols in numerical weather prediction

757   over Europe using the ALADIN-HIRLAM NWP system, Atmos. Res., 172-173,

758   163-173, https://doi.org/10.1016/j.atmosres.2016.01.003, 2016.

759 Toll, V., Reis. K., Ots, R., Kaasik, M., Männik, A., Prank, M., Sofiev, M.: SILAM

760   and MACC reanalysis aerosol data used for simulating the aerosol direct radiative

761   effect with the NWP model HARMONIE for summer 2010 wildfire case in

762   Russia,   Atmos.   Environ.,   121,   75-85,

763   https://doi.org/10.1016/j.atmosenv.2015.06.007, 2015.

764 Wang, H., Shi, G. Y., Zhang, X. Y., Gong, S. L., Tan, S. C., Chen, B., Che, H. Z., and

765   Li, T.: Mesoscale modelling study of the interactions between aerosols and PBL

766   meteorology during a haze episode in China Jing–Jin–Ji and its near surrounding

767   region – Part 2: Aerosols' radiative feedback effects, Atmos. Chem. Phys., 15,

768   3277-3287, https://doi.org/10.5194/acp-15-3277-2015, 2015b.

769   Wang, H., Xue, M., Zhang, X. Y., Liu, H. L., Zhou, C. H., Tan, S. C., Che, H. Z.,

770   Chen, B., and Li, T.: Mesoscale modeling study of the interactions between

771   aerosols and PBL meteorology during a haze episode in Jing–Jin–Ji (China) and

772   its nearby surrounding region – Part 1: Aerosol distributions and meteorological

773   features, Atmos. Chem. Phys., 15, 3257–3275,

774   https://doi.org/10.5194/acp-15-3257-2015, 2015a.

775   Wang, J., Wang, S., Jiang, J., Ding, A., Zheng, M., Zhao, B., Wong, D. C., Zhou, W.,

776   Zheng, G., Wang, L., Pleim, J. E. and Hao, J.: Impact of aerosol–meteorology

777   interactions on fine particle pollution during China's severe haze episode in

778   January 2013, Environ. Res. Lett., 9, 094002, doi:10.1088/1748-9326/9/9/094002,

779   2014.

780   Wang, X, He, X., Miao, S., Dou, Y.: Numerical simulation of the influence of

781   aerosol radiation effect on urban boundary layer, Sci. China Earth Sci., 61, 1844–

782   1858, https://doi.org/10.1007/s11430-018-9260-0, 2018.

783   Yang, X., Zhao, C., Zhou, L., Wang, Y., Liu, X.: Distinct impact of different types of

784   aerosols on surface solar radiation in China, J. Geophys. Res.-Atmos., 121,

785   6459-6471, doi: 10.1002/2016JD024938, 2017b.

786   Yang, Y. and Ren, R. C.: On the contrasting decadal changes of diurnal surface

787   temperature range between the Tibetan Plateau and southeastern China during the

788   1980s–2000s, Adv. Atmos. Sci., 34, 181–198, doi: 10.1007/s00376-016-6077-z,

789 2017a.

790 Yu, H., Kaufman, Y. J., Chin, M., Feingold, G., Remer, L. A., Anderson, T. L.,

791 Balkanski, Y., Bellouin, N., Boucher, O., Christopher, S., DeCola, P., Kahn, R.,

792 Koch, D., Loeb, N., Reddy, M. S., Schulz, M., Takemura, T., and Zhou, M.: A

793 review of measurement-based assessments of the aerosol direct radiative effect

794 and forcing, Atmos. Chem. Phys., 6, 613-666,

795 https://doi.org/10.5194/acp-6-613-2006, 2006.

796 Zaveri, R. A. and Peters, L. K.: A new lumped structure photochemical mechanism

797 for large-scale applications, J. Geophys. Res., 104, 30387–30415,

798 https://doi.org/10.1029/1999JD900876,1999.

799 Zhai, S., Jacob, D. J., Wang, X., Shen, L., Li, K., Zhang, Y., Gui, K., Zhao, T., and

800 Liao, H.: Fine particulate matter ($PM_{2.5}$) trends in China, 2013–2018: separating

801 contributions from anthropogenic emissions and meteorology, Atmos. Chem.

802 Phys., 19, 11031-11041, https://doi.org/10.5194/acp-19-11031-2019, 2019.

803 Zhang, B., Wang, Y., and Hao, J.: Simulating aerosol–radiation–cloud feedbacks on

804 meteorology and air quality over eastern China under severe haze conditionsin

805 winter, Atmos. Chem. Phys., 15, 2387-2404,

806 https://doi.org/10.5194/acp-15-2387-2015, 2015.

807 Zhang, Q., Ma, Q., Zhao, B., Liu, X., Wang, Y., Jia, B., and Zhang, X.: Winter haze

808 over North China Plain from 2009 to 2016: Influence of emission and

809 meteorology, Environ. Pollut., 242, 1308–1318.

810   doi:10.1016/j.envpol.2018.08.019, 2018.

811   Zhang, Q., Quan, J., Tie, X., Li, X., Liu, Q., Gao, Y., and Zhao, D. L.: Effects of

812   meteorology and secondary particle formation on visibility during heavy haze

813   events in Beijing, China, Sci. Total Environ., 502, 578–584,

814   https://doi.org/10.1016/j.scitotenv.2014.09.079, 2015.

815   Zhang, Y., Wen, X.-Y., and Jang, C.-J.: Simulating

816   chemistry-aerosol-cloud-radiation-climate feedbacks over the continental U.S.

817   using the online-coupled Weather Research Forecasting Model with chemistry

818   (WRF/Chem), Atmos. Environ. 44, 3568–3582,

819   https://doi.org/10.1016/j.atmosenv.2010.05.056, 2010.

820   Zhang, Y.-Z, Miao, S.-G., Dai, Y.-J., Liu, Y.-H., Numerical simulation of

821   characteristics of summer clear day boundary layer in Beijing and the impact of

822   urban underlying surface on sea breeze (in Chinese), Chin J. Geophys, 56,

823   2558–2573, 2013.

824   Zhao, X., Li, Z., Xu, J.: Modification and performance tests of visibility

825   parameterizations for haze days, Environ. Sci., 40, 1688-1696 (in Chinese), 2019.

826   Zheng, Y., Che, H., Xia, X., Wang, Y., Wang, H., Wu, Y., Tao, J., Zhao, H., An, J.,

827   Li, L., Gui, K., Sun, T., Li, X., Sheng, Z., Liu, C., Yang, X., Liang, Y., Zhang, L.,

828   Liu, C., Kuang, X., Luo, S., You, Y., and Zhang, X.: Five-year observation of

829   aerosol optical properties and its radiative effects to planetary boundary layer

830   during air pollution episodes in North China: Intercomparison of a plain site and

831   a mountainous site in Beijing, Sci. Total Environ., 674, 140–158.

832   https://doi.org/10.1016/j.scitotenv.2019.03.418, 2019.

833 Table 1. The variables, sources, numbers of sites in the domain/NCP and the

834 frequency of chemical and meteorological observations.

Variables	Source of observation	Numbers of sites over the domain/NCP	Frequency	locations
AOD	AERONET	3/3	hourly	black dots in Fig. 1b
AOD	IAP station	1/1	hourly	blue dot in Fig. 1b
AOD	MODIS	/	daily	Fig. 2f-j and Fig. 2p-t
aerosol extinction coefficient	CALIPSO	/	daily	black paths in Fig.3a-d
$PM_{2.5}$	China National Environmental Monitoring Centre	813/332	hourly	dots in Fig. 5a
radiation	China Meteorological Administration	4/4	hourly	triangles in Fig. 1a
radiation	IAP station	1/1	hourly	triangles in Fig. 1a
2-m temperature	China Meteorological Administration	1157/534	hourly	dots in Fig. 11a
wind at 10m	China Meteorological Administration	1157/534	hourly	dots in Fig. 11a
atmospheric wind	China Meteorological Administration	2/2	0800LT, 2000LT	circles in Fig. 1a

835

836   Table 2. Mean bias of downward SW radiation at surface (W m^{-2}) and Net radiation

837   at surface (W m^{-2}) from NoAero and Aero relative to observation during daytime

838   (averaged 0800 to 1800 LT) and nighttime (averaged 1900 to 0700 LT), averaged

839   from 6th to 11th Dec. 2015 at Beijing, Tianjin, Taiyuan and Jinan respectively.

840

Station	SW radiation		Net radiation			
	Daytime		Daytime		Nighttime	
	NoAero	Aero	NoAero	Aero	NoAero	Aero
Beijing	149.4	38.0	102.2	15.0	-33.6	-33.2
Tianjin	115.5	70.9	72.2	36.4	-27.1	-26.4
Taiyuan	155.0	118.3	66.9	43.2	-33.6	-33.3
Jinan	149.1	97.7	81.2	45.3	-30.3	-29.3

841
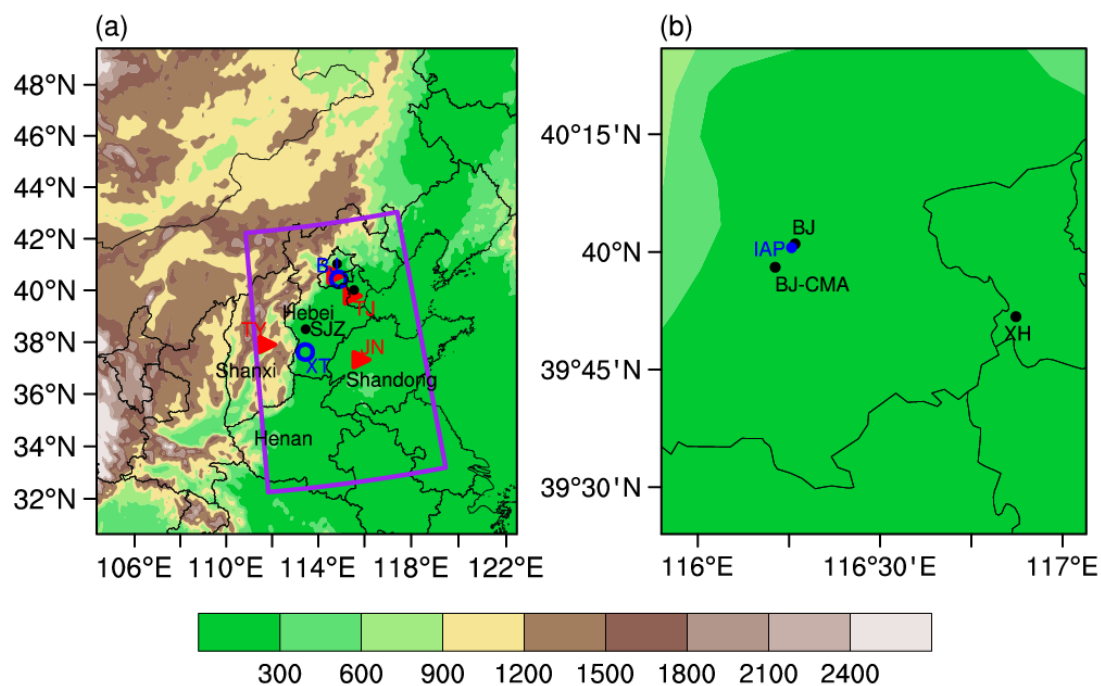
842 Figure 1. (a) The model domain and the terrain height (shadings, m). Purple box

843 denotes the NCP, triangles are the observational sites of radiation (BJ: Beijing, TJ:

844 Tianjin, TY: Taiyuan and JN: Jinan), circles are sites of sounding observation (BJ:

845 Beijing and XT: Xingtai), dots denote the major cities for validation of $PM_{2.5}$ (BJ:

846 Beijing, SJZ: Shijiazhuang and TJ: Tianjin). Names of provinces are also added

847 (Hebei, Shanxi, Shandong and Henan). (b) The observational sites of AOD,

848 including AERONET sites (black dots, BJ: Beijing, BJ-CMA: Beijing-CMA and XH:

849 Xianghe) and IAP in-situ (blue dot) site.

850

851
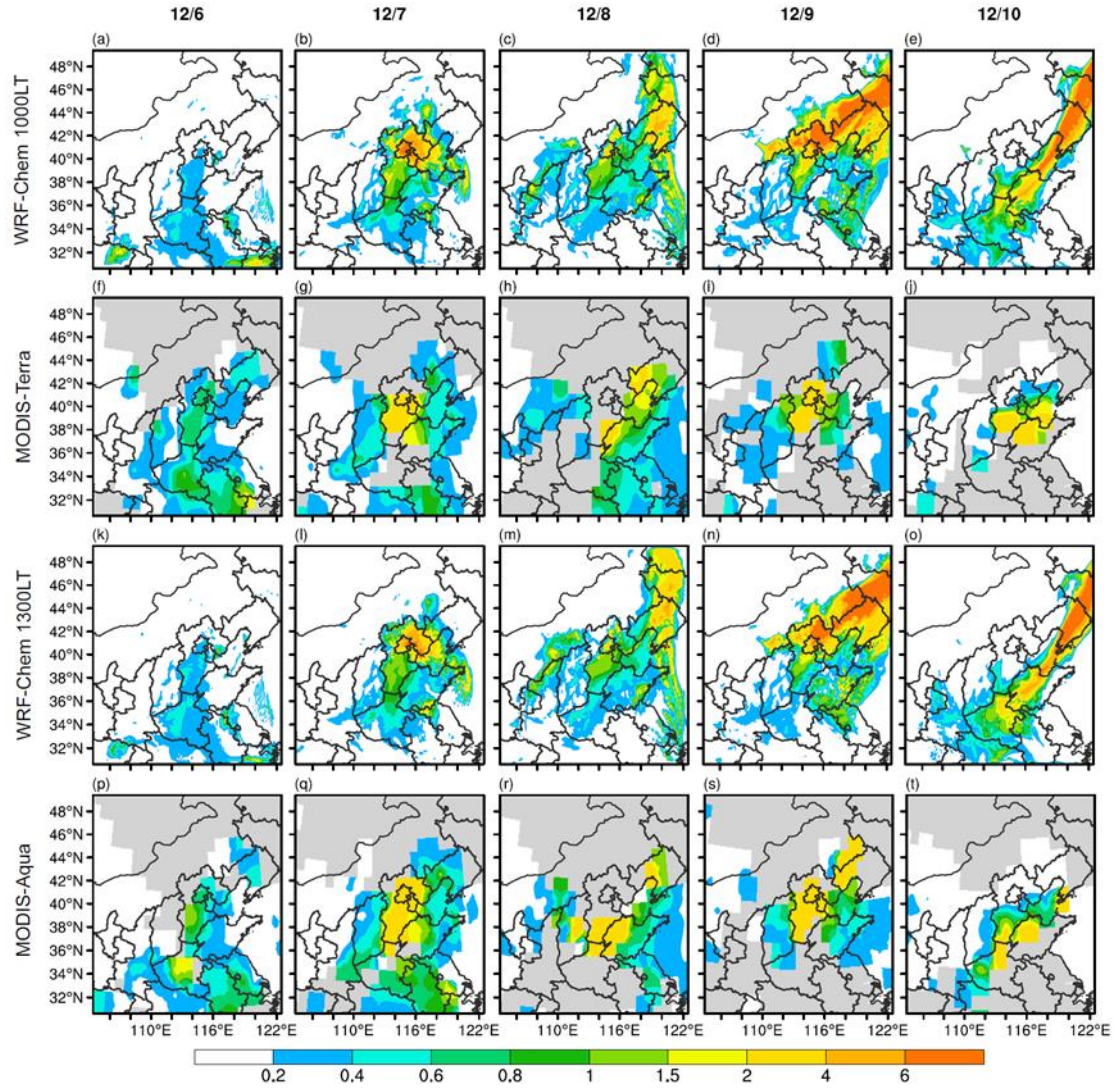
Figure 2. The WRF-Chem simulated and MODIS observed spatial distribution of

AOD on 6th-10th December (from left to right). The first (a-e) and third rows (k-o)

are WRF-Chem simulations at 1000LT and 1300LT (MODIS path times)

respectively. The second (f-j) and fourth (p-t) rows are MODIS Terra and Aqua

observations, respectively. Gray areas in (f-j) and (p-t) denote the missing values.

857

858
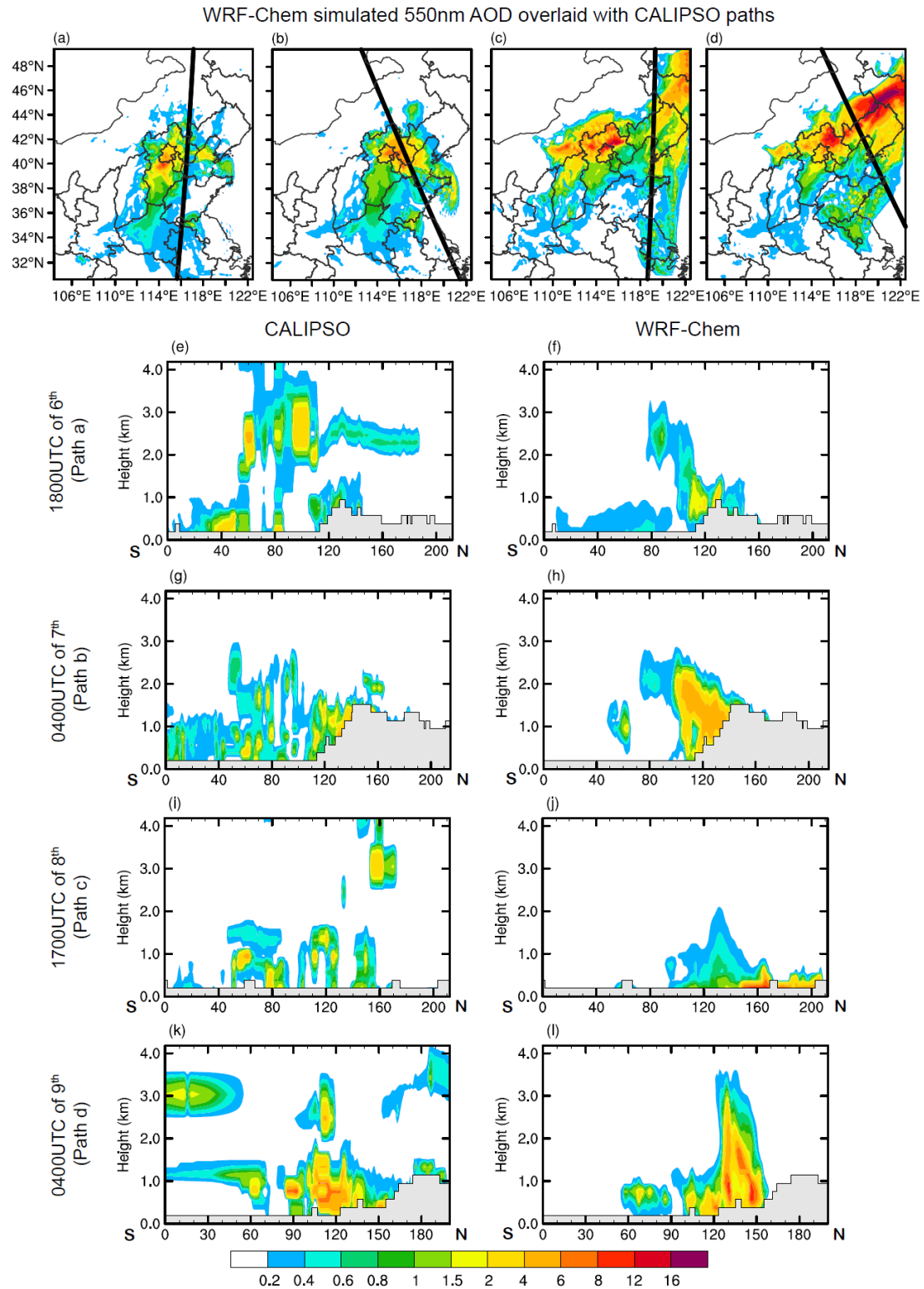
Figure 3. The WRF-Chem simulated 550nm AOD (shadings) on (a)1800UTC of 6th,

(b) 0400UTC of 7th, (c)1700UTC of 8th, (d) 0400UTC of 9th December overlaid with

CALIPSO paths (black thick solid). (e-l) denote the corresponding vertical

862 distributions of aerosol extinction coefficient at 550nm from (e, g, i, k) CALIPSO and

863 (f, h, j, l) model simulations. Gray areas in (e-l) denote the terrain.

864

865
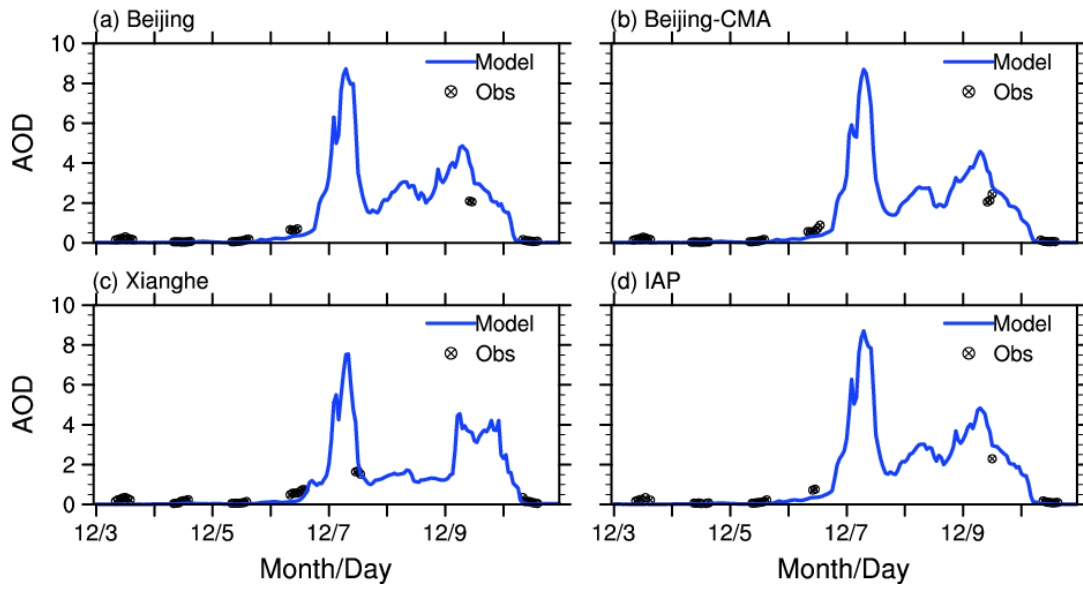
866 Figure 4. Temporal variation of observed (black dots) and simulated (blue) AOD at

867 550nm during 3rd-10th Dec. (LT) at (a) Beijing, (b) Beijing-CMA, (c) Xianghe and (d)

868 IAP, AOD observations are from (a-c) AERONET and (d) IAP in-situ site.

869

870
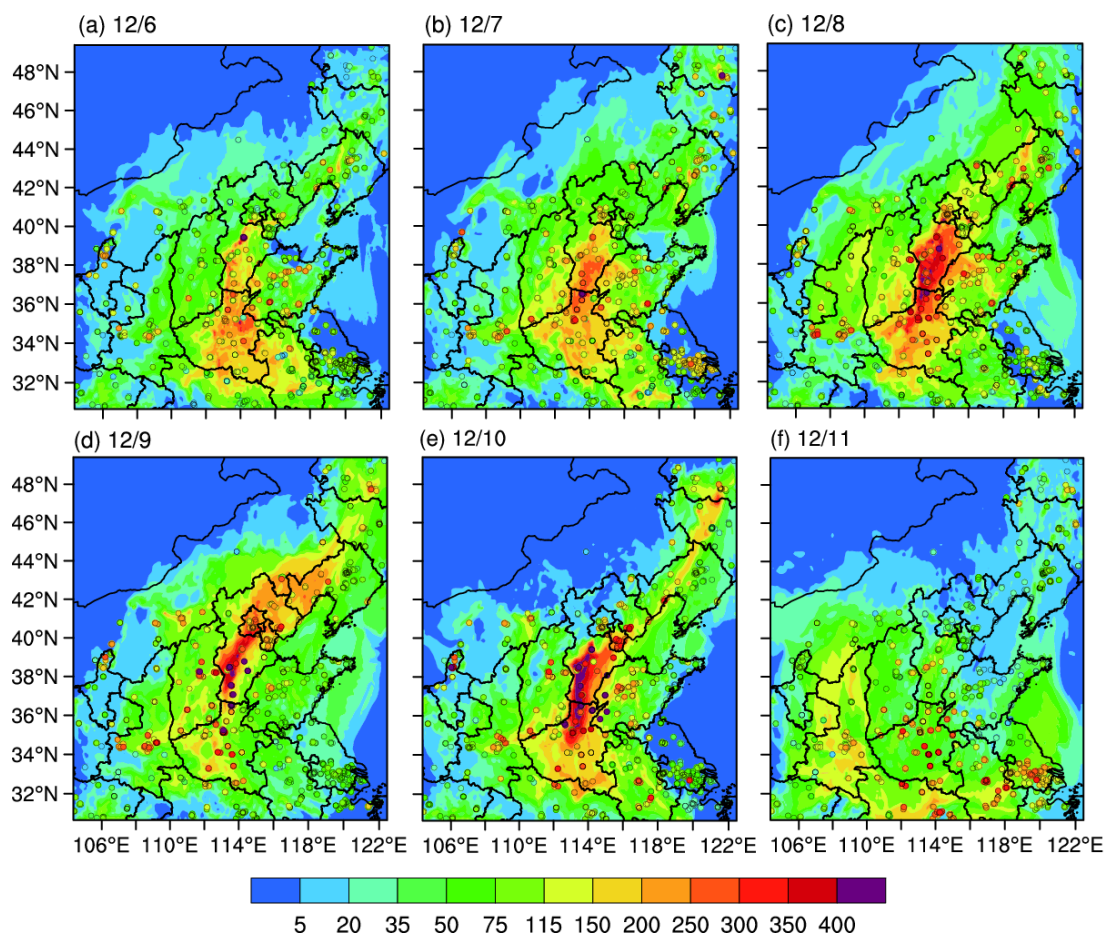
Figure 5. Observed (colored dots) and WRF-Chem simulated (shadings) spatial

distribution of PM$_{2.5}$ concentrations (μg m^{-3}) on 0800LT of (a) 6th, (b) 7th, (c) 8th, (d)

9th, (e) 10th and (f) 11th Dec. respectively.

874
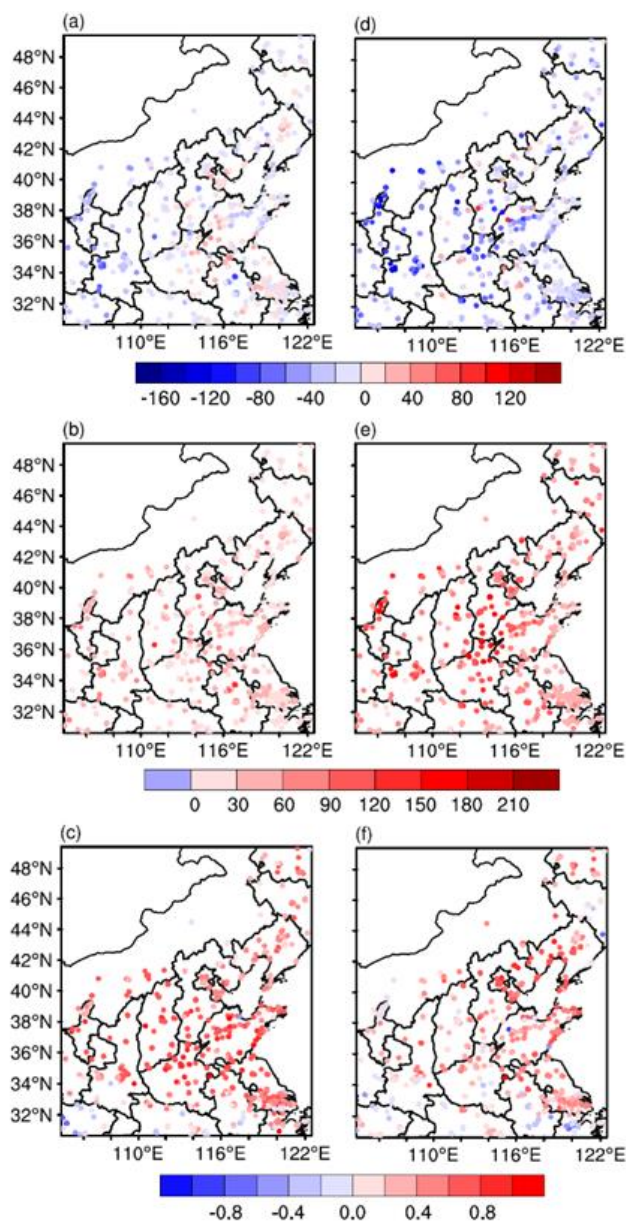
875

876 Figure 6. The (a, d) bias (μg m^{-3}), (b, e) RMSE (μg m−3), and (c, f) correlation

877 coefficient (1) averaged (a-c) during clean period (3th to 5th Dec.) and (d-f) the

878 polluted period (6th to 10th December).

879
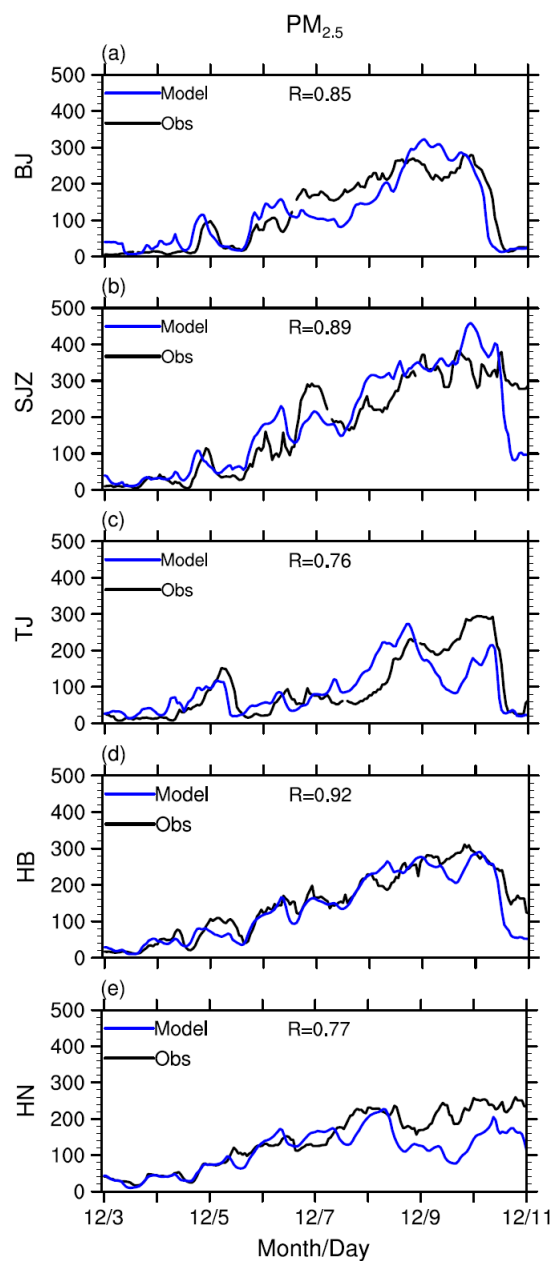
880

881 Figure 7. Observed (black) and WRF-Chem simulated (blue) temporal variation of

882 PM$_{2.5}$ (μg m^{-3}) at three major cities (a) Beijing (BJ), (b) Shijiazhuang (SJZ)

883 (c)Tianjin (TJ) and two provinces (d) Hebei (HB) and (e) Henan (HN).

884

885
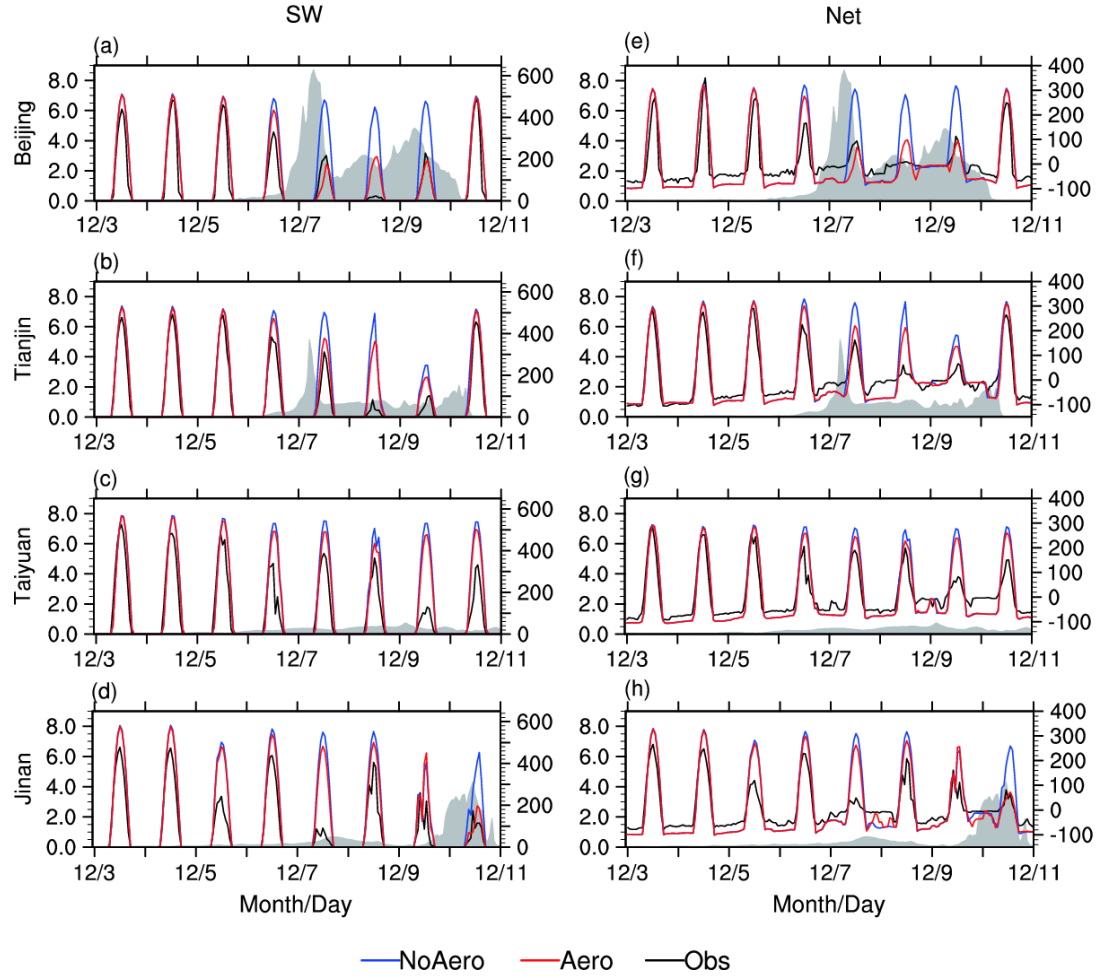
Figure 8. (a–d) observed (black) and WRF simulated (NoAero: blue, Aero: red)

886

temporal variation of   downward shortwave radaition at surface (W m^{-2}, right axis)

887

at (a) Beijing, (b) Tianjin, (c) Taiyuan and (d) Jinan, respectively. The grey areas

888

indicate the simulated AOD (left axis) by WRF-Chem. (e–h) are same with (a–d),

889

but for net radaition at surface (W m^{-2}).

890

891
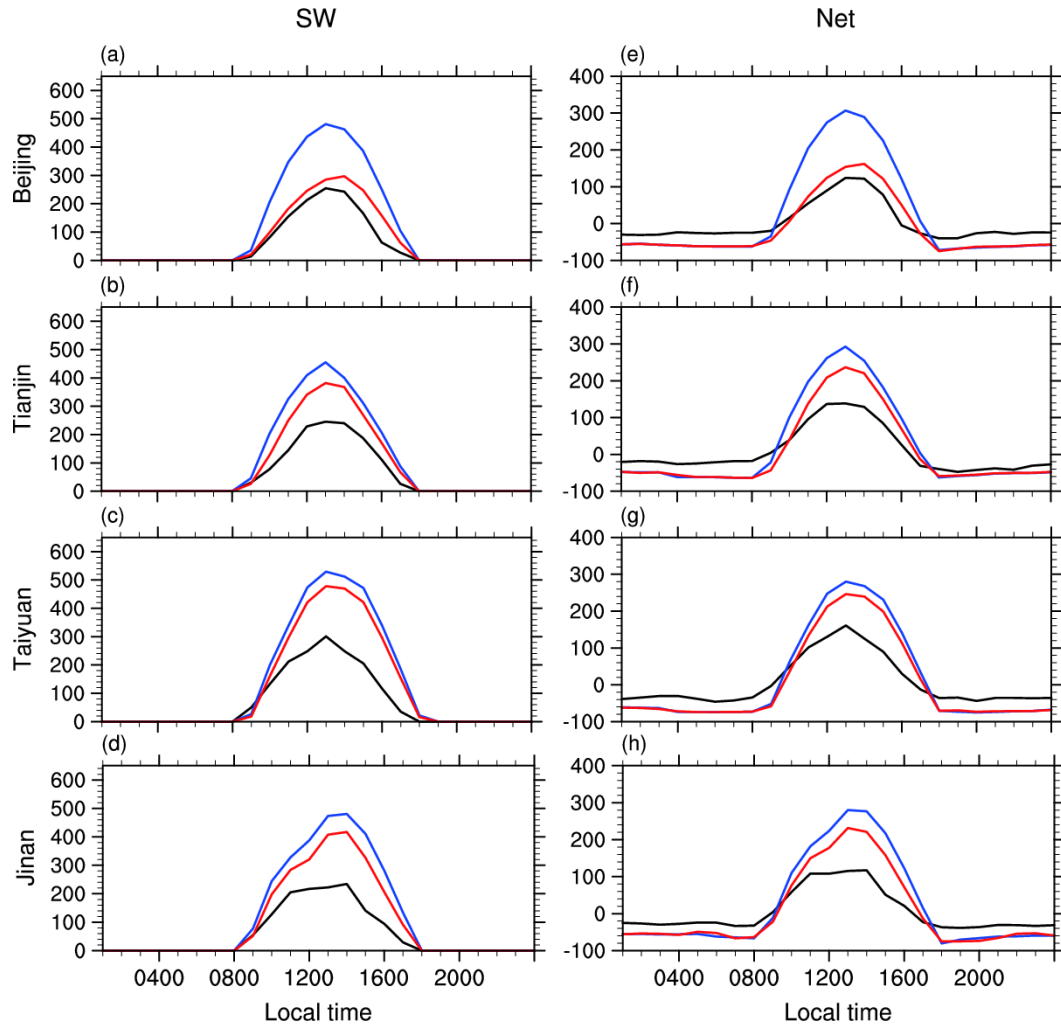
Figure 9. (a–d) observed (black) and simulated (NoAero: blue, Aero: red) diurnal

cycles of downward shortwave radaition at surface (W m^{-2}) averaged from 6th to 10th

Dec. 2015 at (a) Beijing, (b) Tianjin, (c) Taiyuan and (d) Jinan, respectively. (e–h)

are same with (a–d), but for net radaition at surface (W m^{-2}).
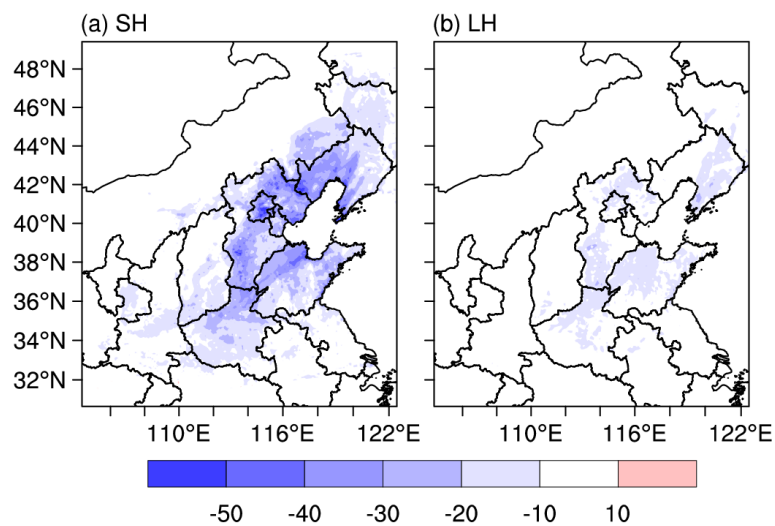
896

897   Figure 10. The differences (Aero minus NoAero) of (a) surface sensible heat flux

898   and (b) surface latent heat flux (W m^{-2}, upward is positive) at 1300LT averaged

899   from 6th to 10th Dec. 2015.
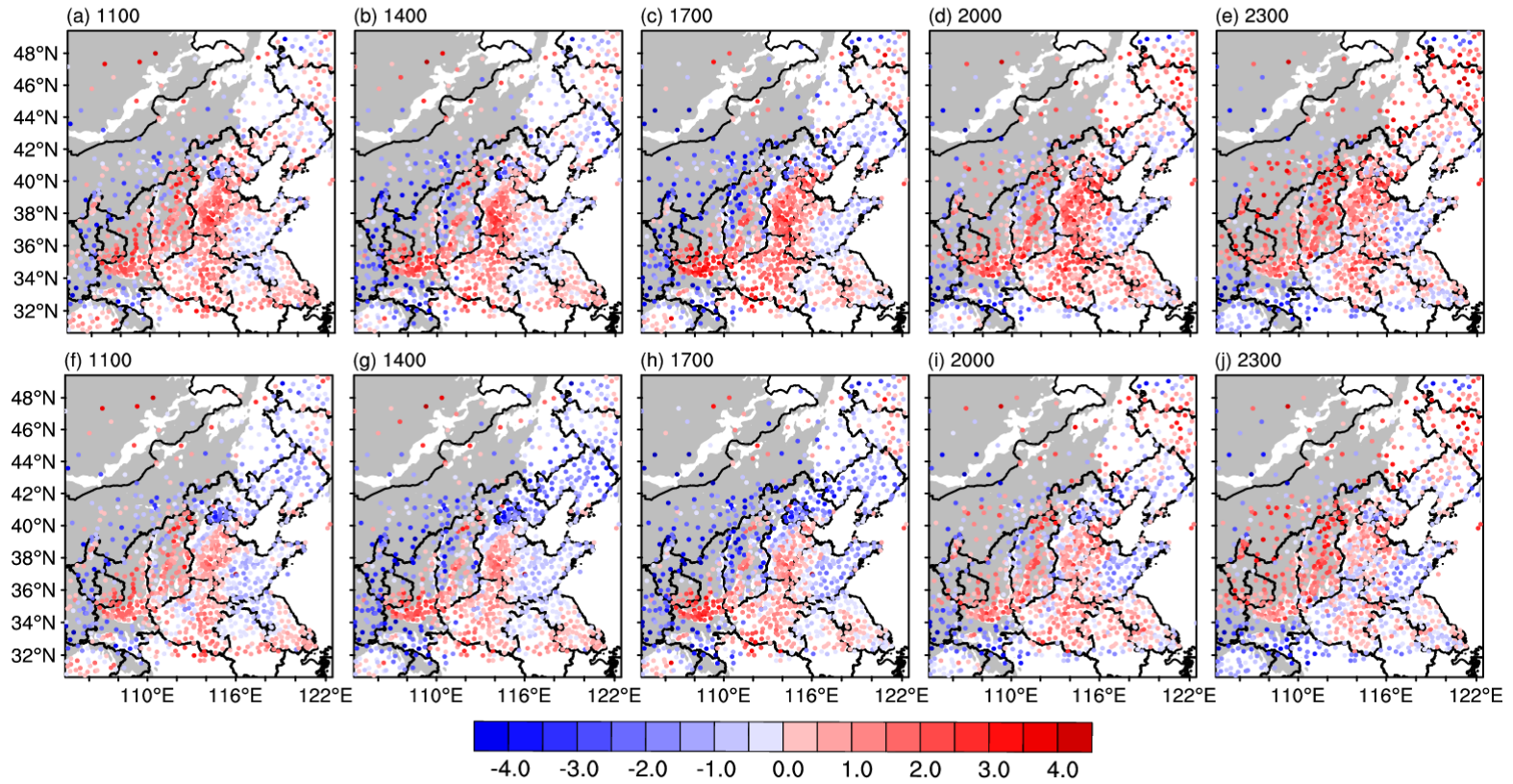
900

901   Figure 11. The bias of 2-m temperature (°C) at (a) 1100, (b) 1400, (c) 1700, (d) 2000 and (e) 2300 LT in NoAero averaged from 6th to 10th Dec.

902   2015, (f–j) are same with (a–e), but for Aero. The grey areas denote the areas of terrain height above 1000m.

903
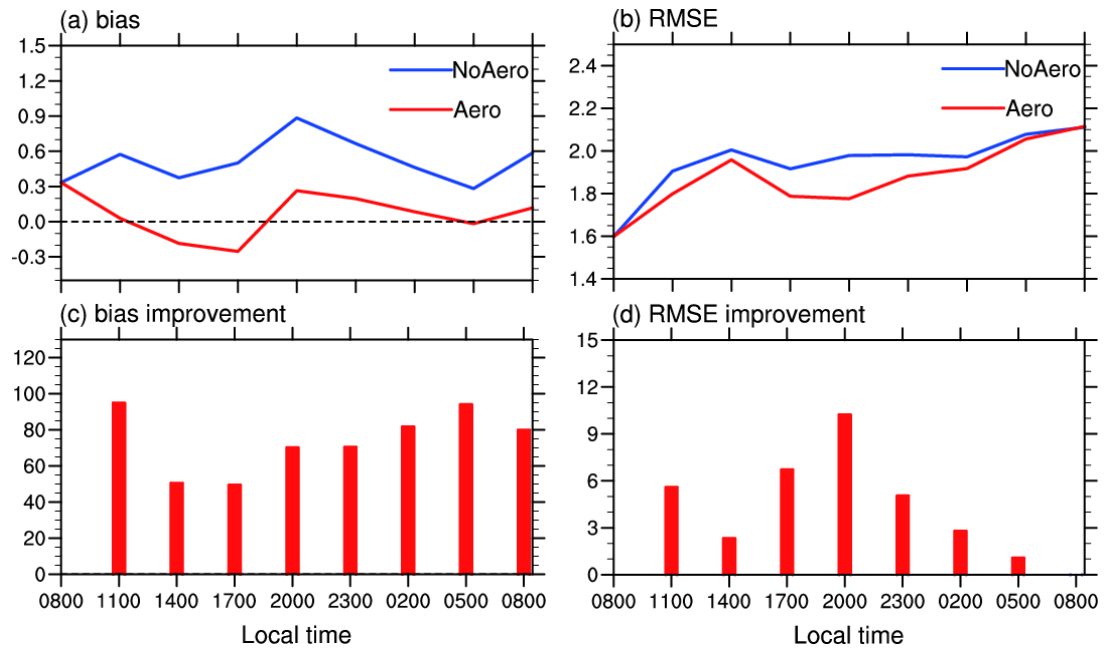
904   Figure 12. Area-averaged (a) bias and (b) RMSE of simulated 2-m temperature (°C)

905   in NoAero (blue) and Aero (red) over NCP area (defined in Fig. 1a), averaged from

906   6th to 10th Dec. 2015, and the mean improvement (%) of (c) absolute value of bias

907   and (d) RMSE in Aero relative to NoAero.

908
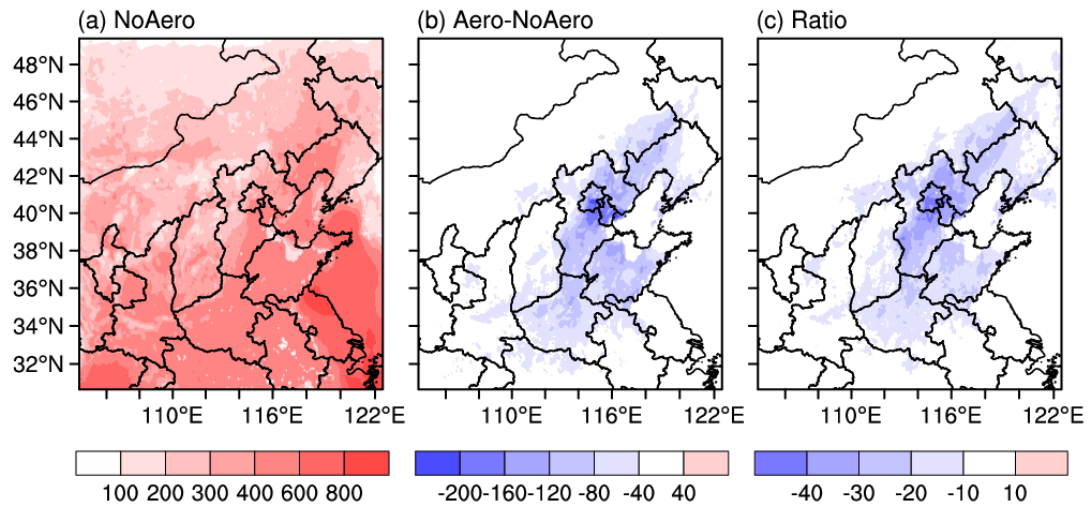
909 Figure 13. Daytime mean PBLH (m) in NoAero, (b) the difference between Aero

910 and NoAero (Aero minus NoAero) and (c) the ratio of changes (%) averaged during

911 6th to 10th Dec. 2015.
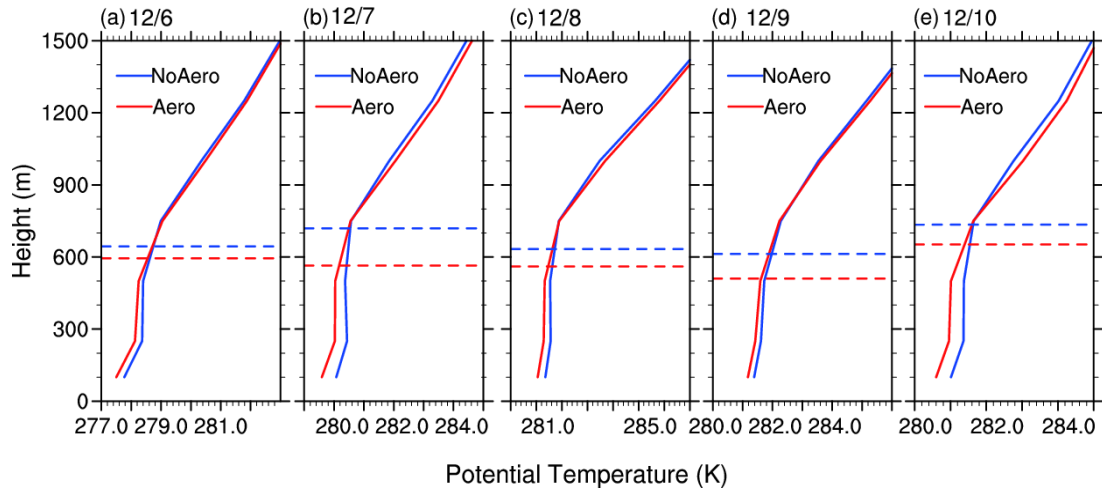
912

913   Figure 14. NCP (defined in Fig. 1a) area-averaged vertical profiles of potential

914   temperature (K, solid) and planetary boundary-layer height (m, dash) in NoAero

915   (blue) and Aero (red) at 1400 LT of (a) 6th, (b) 7th, (c) 8th, (d) 9th and (e) 10th Dec.

916   2015.
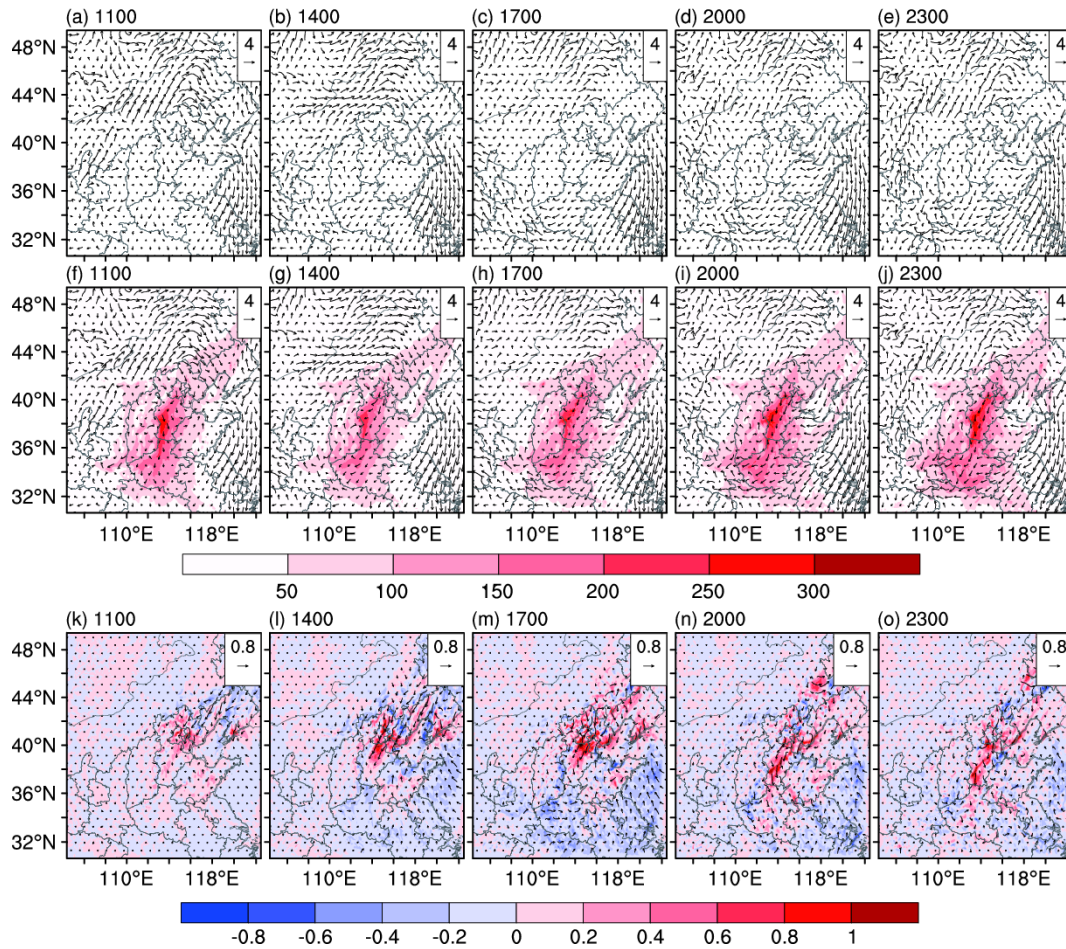
917

918 Figure 15. The 10m wind (vector) at 1100, 1400, 1700, 2000 and 2300 LT in (a–e)

919 NoAero and (f–j) Aero averaged during 6th to 10th Dec. 2015, shadings in (f–j) are

920 simulated $PM_{2.5}$ concentrations ($\mu g\ m^{-3}$). (k–o) the difference of 10m wind (vector)

921 and wind speed (shadings) between Aero and NoAero (Aero minus NoAero).

922
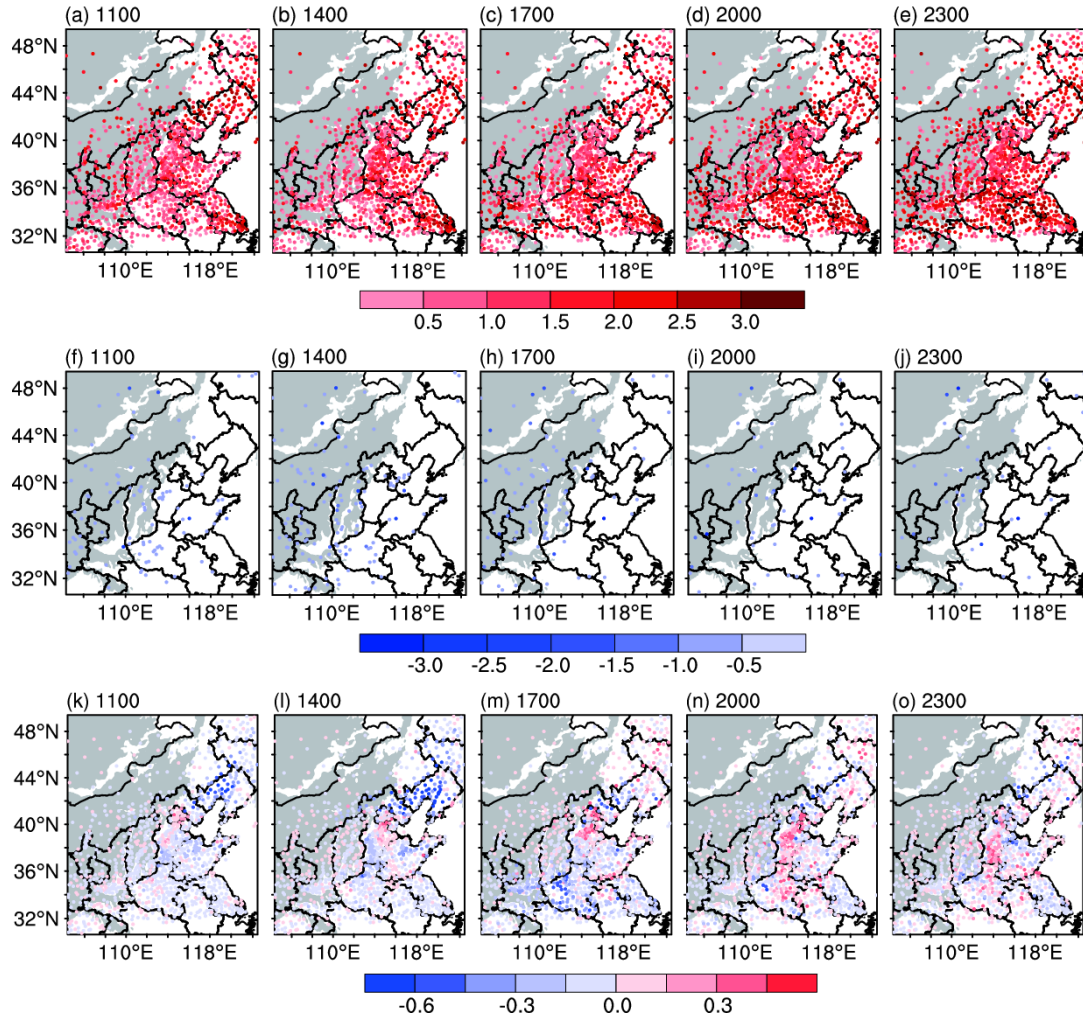
923 Figure 16. The bias of 10m wind speed (m s^{-1}) at 1100, 1400, 1700, 2000 and 2300

924 LT for (a–e) overestimated sites and (f–j) underestimated sites in NoAero averaged

925 during 6th to 10th Dec. 2015.   (k–o) the difference of absolute value of bias (m s^{-1})

926 between Aero and NoAero (Aero minus NoAero). The grey areas denote the areas of

927 terrain height above 1000m.
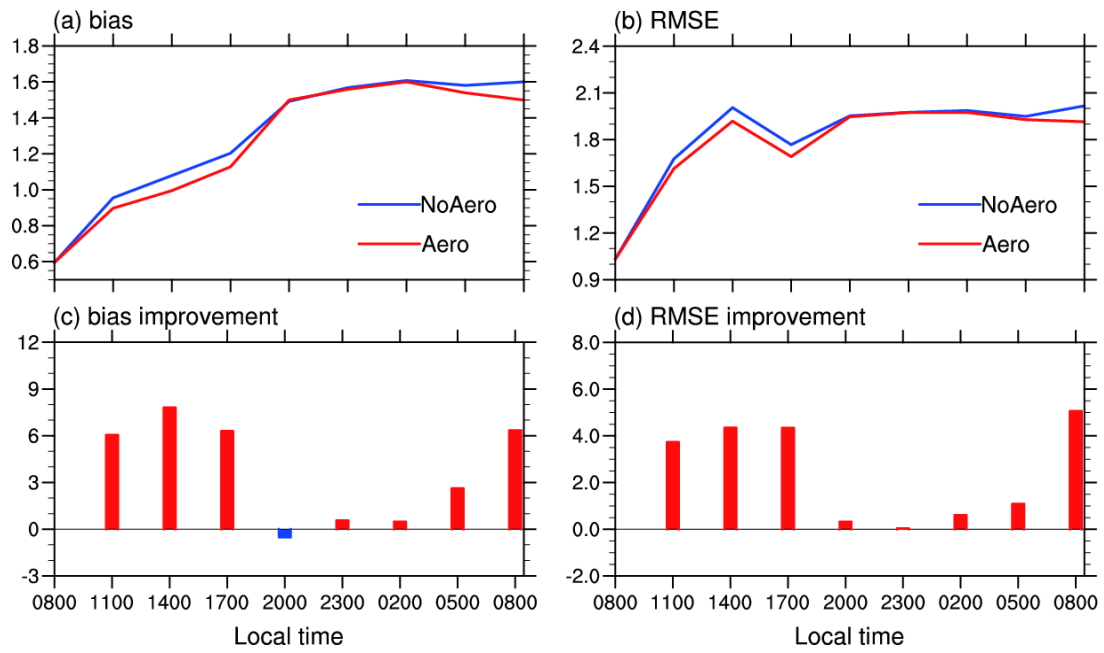
928

929 Figure 17. Same with Fig.12, but for wind speed at 10m (m s^{-1}).
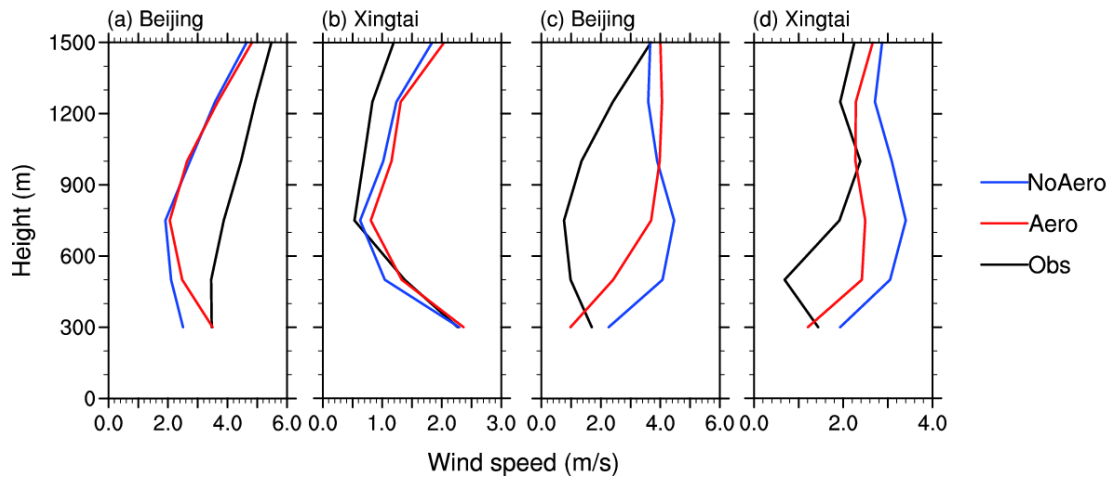
930

931 Figure 18. (a–b) Observed (black) and simulated (NoAero: blue, Aero: red) vertical

932 profiles of atmospheric wind speed (m s^{-1}) at (a) Bejing and (b)Xingtai at 0800LT

933 averaged from 6th to 10th Dec., (c–d) are same with (a–b), but at 2000LT.

934
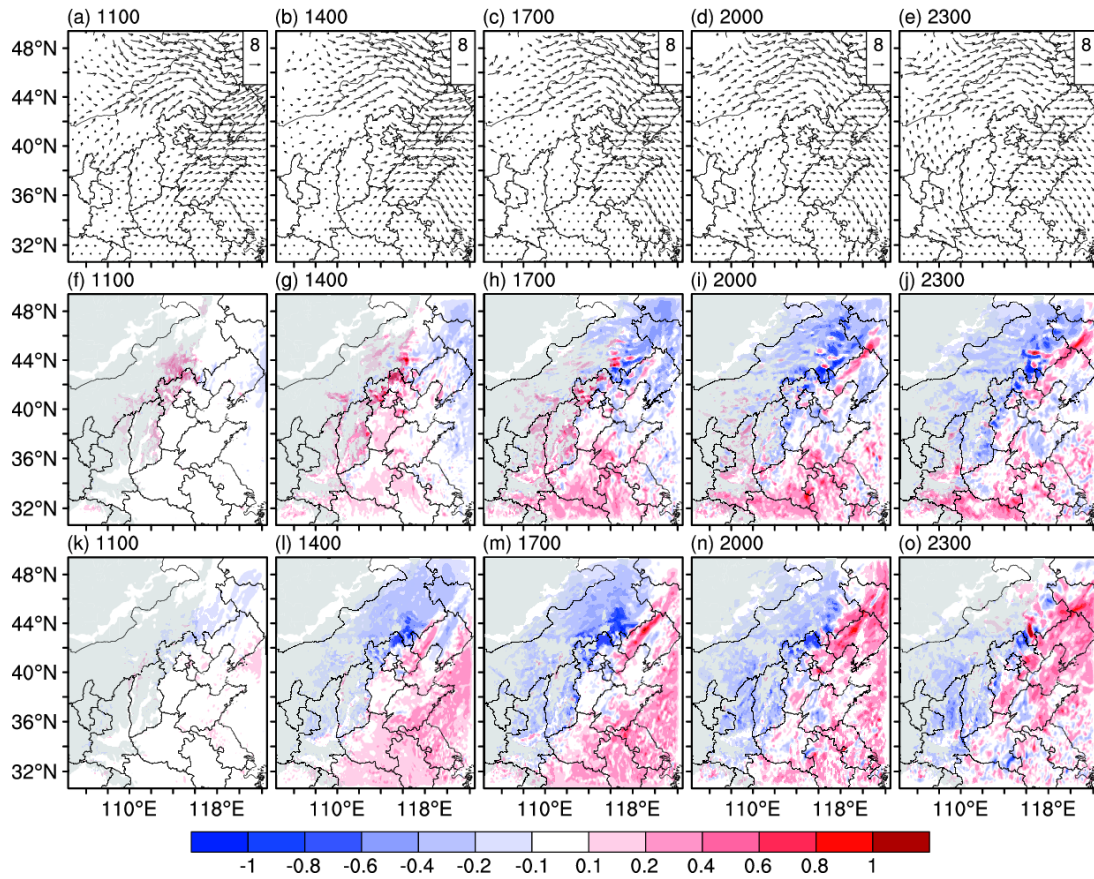
Figure 19. The wind at 850hPa (vector) at 1100, 1400, 1700, 2000 and 2300 LT in

NoAero averaged during 6th to 10th Dec. 2015. The difference of (f–j) U and (k–o) V

wind speed between Aero and NoAero (Aero minus NoAero). The grey areas denote

the areas of terrain height above 1000m.